Journal of Constructional Steel Research 196 (2022) 107409

Contents lists available at ScienceDirect

Journal of Constructional Steel Research

journal homepage: www.elsevier.com/locate/jcsr

Vertical component effects of earthquake and soil-structure interaction on steel gabled frames

Mohammad Malekizadeh [a], Nader Fanaie [b,*], Ali Akbar Pirasteh [c]

[a] Department of Civil Engineering, Academic Center for Education, Culture and Research, Khuzestan Branch, Ahvaz, Iran
[b] Department of Civil Engineering, K. N. Toosi University of Technology, Tehran, Iran
[c] Department of Civil Engineering, Faculty of Engineering, Shahid Chamran University of Ahvaz, Ahvaz, Iran

ARTICLE INFO

Keywords:
Wide-span steel gabled frames
Vertical component of earthquake
Soil-structure interaction
Incremental dynamic analysis
Fragility curves
Probabilistic seismic demand analysis

ABSTRACT

With an increase in the width of the steel gabled frame (SGF) span, in general, the structural mass considerably increases, as a result of which the vertical ground motions can exert significant inertial force on the members of a structure. Although numerous studies have confirmed the destructive effects of the vertical component of earthquake on concrete and steel structures, no research has been devoted to the impact of this component on steel gabled structures yet. Hence, the findings of this research will, at best, unveil possible new dimensions of these types of structures. Moreover, the investigation into the behavior of such structures with regard to the effects of soil-structure interaction (SSI) can help gain a more accurate understanding of their behavior. To this aim, in the present paper, an incremental dynamic analysis (IDA) was conducted for the first time on four SGFs with spans of 20 m and 60 m and heights of 6 m and 12 m with and without consideration of the vertical component of earthquake as well as SSI. Results were collected in the form of multi-record IDA curves, summarized IDA curves, fragility curves and probabilistic seismic demand analysis (PSDA) curves, indicating that the vertical component of earthquake had a determinative role on the seismic performance of wide-span SGFs. This component causes the structure to reach the nonlinear region more quickly, raises the stiffness changes in the nonlinear region, enlarges the data dispersion and demand sensitivity, intensifies the softening behavior, reduces the dynamic capacity, raises the failure probability, enhances the uncertainty, increases the mean annual frequency (MAF) and accelerates the damage in such structures. However, SSI does not have any significant role in the seismic performance of SGFs; just partially leading to more conservative results, especially when they have wide spans. Besides, the results of the PSDA analysis showed that under similar conditions, short-period SGFs are more vulnerable than long-period SGFs and should be prioritized for retrofitting.

1. Introduction

Industrial buildings are one of the main components of industrial growth in a country. The recent technological advances in the areas of construction techniques and building materials and design theories have enabled designers to use steel gabled frame (SGF) systems for wide-span industrial buildings so that they are rapidly expanding in developed countries and have numerous applications. Instances of such structures are aircraft hangars, industrial factories, warehouses, sports complexes, conference halls, pools, etc. SGFs are built and implemented in single-, two-, and multi-span forms; among them, single-span SGFs are more common and enjoy greater applicability because of creating a space for the passage of giant vehicles such as aircrafts, creating structures with unique architecture, advantageous structural style, etc.

SGFs do not have significant ductility due to their low degree of indeterminacy, and with the formation of a small number of plastic hinges, instability occurs in these types of structures. For this reason, nonlinear analysis is not much common for the SGFs, but due to the fact that these structures are very sensitive to the formation of plastic hinges, it is necessary to investigate their behavior in the nonlinear region and it seems that the use of incremental dynamic analysis (IDA), which consists of a large number of nonlinear time-history analyses under a set of ground motion records, is a good option for them. On the other hand, ground motions and their effects on structures are probabilistic

* Corresponding author at: K. N. Toosi University of Technology, Civil Engineering Department, No. 1346, Vali-Asr Street, P.O. Box. 15875-4416, 19697 Tehran, Iran.
E-mail addresses: mohammadmalekizadeh@yahoo.com (M. Malekizadeh), fanaie@kntu.ac.ir (N. Fanaie), pirasteh@scu.ac.ir (A.A. Pirasteh).

https://doi.org/10.1016/j.jcsr.2022.107409
Received 28 August 2021; Received in revised form 24 June 2022; Accepted 26 June 2022

inherently. Accordingly, adopting probabilistic approaches to estimate the expected response of structures under future ground motions is more emphasized. In this regard, performance-based earthquake engineering (PBEE) is a well-known technique for incorporating probabilistic parameters in the seismic assessment of new and existing structures [1]. To this aim, PBEE uses the probabilistic seismic demand analysis (PSDA) to calculate the mean annual frequency (MAF) of exceeding a response parameter for a given structure at a designated site. Various sources of uncertainty (e.g., record to record uncertainty, etc.) can be incorporated into this analysis [2,3].

Considering the fact that the steel gabled structures are classified as lightweight structures, in most cases, not only their horizontal component of earthquake but also their vertical component is disregarded. However, upon an increase in the SGF span, structural mass significantly increases. Consequently, the vertical ground motions can cause large inertial forces in the structural members. Hence, the study of the seismic performance of wide-span SGFs under such ground motions is of great importance due to the heavy cost of industrial equipment and the significant number of people working in these structures and is a key issue in any high seismic zone.

Intense vertical ground motions have been observed in earthquakes occurring in the previous decades [4–7] and destructive effects have been reported for such motions [8]. Significant damage to the piers of a bridge [9,10], brittle failure of reinforced concrete columns [11], decreased shear capacity of vertical structural members [12,13], and even collapse of structures [14] are some possible effects of the vertical ground motions. According to reports, in bridges, it may lead to pounding and vertical separation of girder from bearing. Moreover, increasing axial forces in piers and damage to decks are other possible outcomes mentioned in the literature [15,16]. Some recent studies on the conventional frame structures have indicated that the vertical component of earthquake can change the structural collapse mechanisms [17] as well as increase the vertical acceleration demands of the column lines and beam deformation demands [18,19]. Moreover, the destructive and undesirable effects of the vertical component of earthquake on the base-isolated systems in conventional structures were investigated [20,21]. Research has shown that the vertical component of earthquake increases the nonlinear vertical displacement [22] and the demand/capacity ratio [23] in masonry structures. The destructive impact of the vertical component of earthquake on the tanks has also been addressed [24,25]. It has been reported that the vertical component of earthquake leads to a significant rise of the axial force in the central columns and even collapse of the underground structures [26,27]. Further to the above-mentioned researches, many numerical and experimental studies have highlighted the structural damages due to the effects of the vertical component of earthquake.

Given that steel gabled structures are considered to be light structures, almost all studies have disregarded the effects of Soil-Structure Interaction (SSI). However, it is noteworthy that when a structure is implemented in soft soil, SSI may exert a significant influence and even lead to instability of the structure. Hence, considering SSI can help achieve a better understanding of the investigations into the behavior of such structures.

Research dealing with SSI has been extensively conducted since the 1970s [28–31]. Such studies have pointed to the significant changes in the seismic performance of bridges under the SSI effect [32–34]. Furthermore, incorporating SSI in conventional buildings in soft soil can lead to a meaningful increase in the structural response [30,35]. In some recent investigations, incorporating SSI in towers has led to increasing residual settlements [36], natural period and overall deformation of the structure [37] so that the most important factor in lengthening their natural period is the rotation of the foundation [28]. Moreover, considering SSI in nuclear reactors increases the fundamental period [38,39] and raises the roof drift demand of the structure [40]. In wind turbines, incorporating SSI enhances the background response [41] as well as leads to horizontal acceleration and displacement increase at the top of the nacelle [42].

Although a review of the literature corroborates the destructive effects of the vertical component of earthquake and SSI on the above-mentioned structures, there is no study dealing with such effects on steel gabled structures and the present study is hoped to offer a new perspective to the research in this field. To this aim, four SGFs with spans of 20 m and 60 m and heights of 6 m and 12 m undergo IDA analysis in this study for the first time with and without consideration of the vertical component of earthquake as well as SSI. The results will be presented in the form of multi-record IDA curves, summarized IDA curves, fragility curves, and PSDA curves. A general flowchart for the present research is given in Fig. 1. Also, the major advantages of this study are the following:

1. Presenting the multi-record IDA curves for the SGFs for the first time;
2. Evaluation and comparison of the effect of the vertical component of earthquake and SSI on the seismic behavior of SGFs from the linear

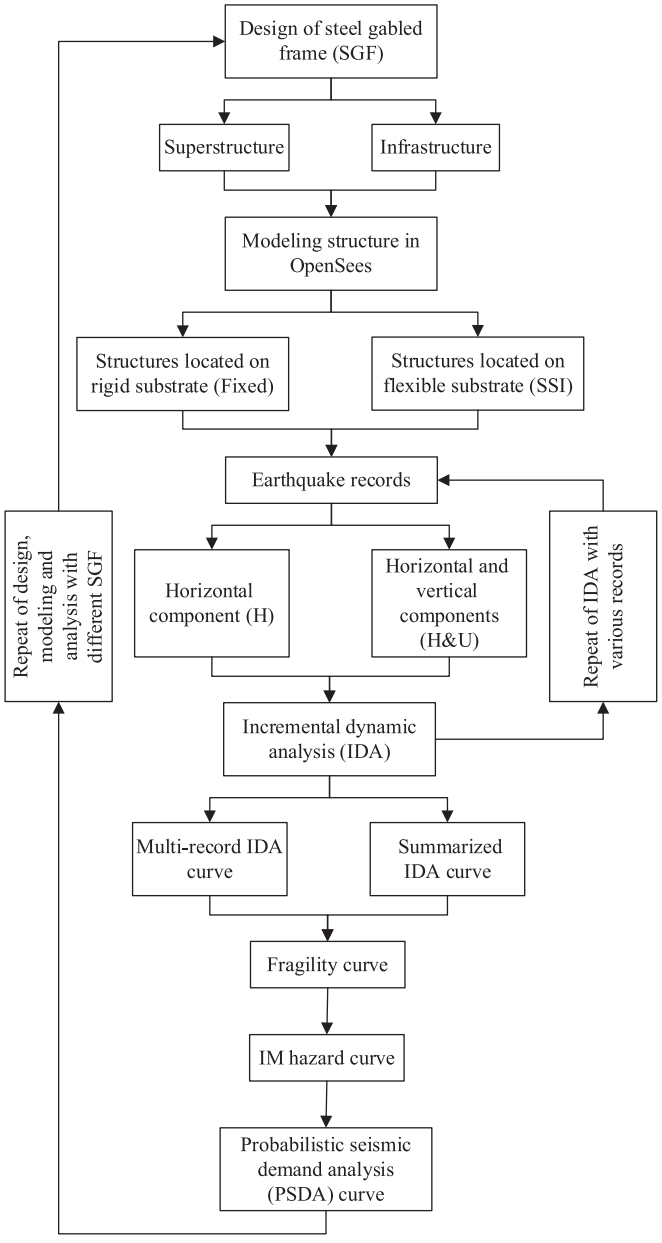

Fig. 1. General flowchart of the present study.

region up to the collapse level with the help of multi-record IDA curves;
3. Presenting the summarized IDA curves for the SGFs for the first time;
4. Evaluation and comparison of the effect of the vertical component of earthquake and SSI on the dynamic capacity of SGFs with the help of summarized IDA curves;
5. Presenting the fragility curves for the SGFs for the first time;
6. Evaluation and comparison of the effect of the vertical component of earthquake and SSI on the failure probability of SGFs with the help of fragility curves;
7. Presenting MAF for the SGFs for the first time;
8. Evaluation and comparison of the effect of the vertical component of earthquake and SSI on the MAF of SGFs; and
9. Presenting the PSDA curves for the SGFs for the first time, which can form a basis for the estimation of the probabilistic seismic demand and performance-based design of such structures.

2. Geometrical specifications of the studied models

2.1. Structure

In the present paper, four 2D SGF models are utilized with different spans and heights to analyze and investigate the effects of the vertical component of earthquake and SSI. The span width of models A, B, C and D are 20, 20, 60 and 60 m, respectively, and their column heights are 6, 12, 6 and 12 m, respectively. The geometric characteristics of the studied models are shown in Fig. 2. As can be seen, the entire length of the columns and the region with a length of span/10 in rafters from the eave line (l_{cr}) are characterized by non-prismatic members, while the rest of the length of the rafters up to the ridge is prismatic. In addition, the slope of the roof is considered at 20%. The foot of the columns enjoys hinge support.

The used steel was of ST37 type with the elasticity modulus of 2.039E+10 kgf/m^2. In all of the studied models, an ordinary moment frame was incorporated as the lateral force resisting system. The location for modeling was assumed to be Tehran, Iran, a high seismic zone. The gravity loads applied to the studied models were dead load, balanced snow load, and unbalanced snow load. Walls and roofs were covered with sandwich panels with a weight of 360 kgf/m. ASCE/SEI 7–10 code [43] was used for gravity and lateral loading. The models were designed based on the load and resistance factor design (LRFD) method in line with AISC 360–10 and AISC 341–10 codes [44,45]. Upon the end of the designing process and by employing the trial-and-error approach to achieve an economical model, the section dimensions of the rafter and column members were identified, which are given in Table 1. It is worth mentioning that in the shoulder, the dimensions of the flange and the web were determined in such a way that the section was compact.

2.2. Infrastructure (footing and soil)

Shear wave velocity at the top 30 m (V_{S30}) in northern Tehran is >760 m/s (class A and B soils), while it is between 180 and 360 m/s in the south (class D soil) [46,47]. Since the influence of SSI is more evident on soft soil, in the present paper, the soil beneath the footing of the structure is considered to be of class D. Accordingly, silty sand with the properties given in Table 2 is chosen for the analyses [48].

The elasticity modulus of concrete is assumed equal to 22 GPa and the footing is designed through the limit state method on the basis of ACI 318–14 code [49]. Section dimensions of the footing are given in Table 3.

3. Nonlinear modeling

For nonlinear modeling and analyzing the soil, footing, and structural systems, the OpenSees software [50], an open-source software utilized in the simulation of the seismic response of structural and geotechnical systems, was employed. The software seems promising as an important means of modeling and analyzing both the linear and nonlinear behaviors of structural systems. The following sections of the present study discuss the modeling of soil, footing, and structural systems in detail.

Table 1
Section dimensions of the rafter and column members.

Component	Model A	Model B	Model C	Model D
Column web height at top (m)	0.8	1	1.5	1.5
Column web height at bottom (m)	0.3	0.3	0.3	0.3
Rafter web height at ridge (m)	0.4	0.5	1	1
Rafter web height at eave (m)	0.8	1	1.5	1.5
Web thickness (m)	0.008	0.01	0.014	0.014
Flange thickness (m)	0.01	0.012	0.018	0.02
Flange width (m)	0.18	0.24	0.34	0.4

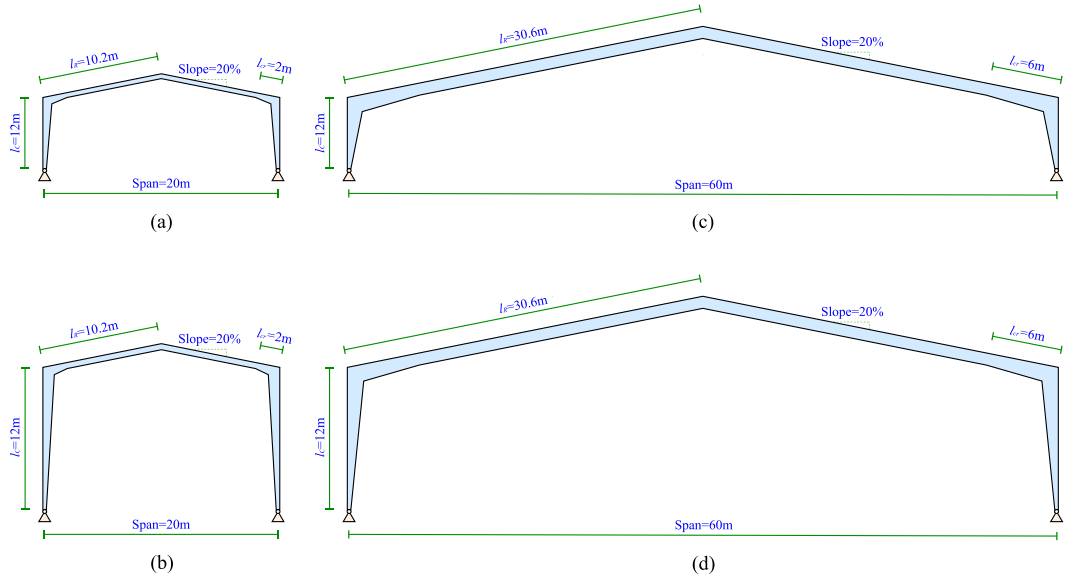

Fig. 2. Geometrical dimensions of (a) model A, (b) model B, (c) model C and (d) model D.

Table 2
Soil properties [48].

Unit weight (kN/m^3)	Friction angle	Shear modulus (MN/m^2)	Poisson's ratio	Cohesion (kN/m^2)	Radiation damping	Tension capacity
18	36°	50	0.35	5	0.05	0.1

Table 3
Section dimensions of the footing.

	Model A	Model B	Model C	Model D
Length (m)	1.2	1.2	3.2	2.4
Width (m)	1.2	1.2	3.2	2.4
Height (m)	0.6	0.6	1.6	1.2

3.1. Structure

OpenSees was employed in the 2D modeling of the structures. For the first time a model of SGFs with web-tapered members was developed using prismatic microelements with variable height on the OpenSees platform. For modeling the viscous damping, Rayleigh damping was adopted [51]. In order to transfer the stiffness and resisting force of the rafter from the basic system to the general coordinate system in a totally accurate way through geometric transformation, the corotational transformation was applied. The nonlinear behavior of the materials in the rafters and columns was modeled using a *nonlinear beam-column element* with distributed plasticity. To this aim, in the OpenSees materials library, *steel01* material with kinematic hardening of 0.02 was selected and the fiber section was assigned to the rafter and column elements, which using defined nonlinear materials enables the nonlinearization of all the components of such sections. This material has a bilinear backbone curve with a post-yield stiffness expressed as a proportion of the initial modulus of elasticity of the steel and accounts for the Bauschinger effect. Also, since the vertical component of earthquake is investigated in this study, due to changes in the axial force of the elements, it is necessary to consider the axial force-moment interaction, which using the fiber method seems to be a good option. In addition, shear deformations are also accounted for. It should be noted that deterioration in the elements can be modeled using the plastic hinge models accepted by guidelines such as FEMA 356 [52], but at present the relationships of this method exist only for prismatic elements. Also, in the fiber method, the parameters related to the cyclic deterioration of materials for non-prismatic elements in order to accurately predict the deterioration of these types of elements are not currently developed in the literature. Therefore, since the relationships and parameters representing the deterioration of non-prismatic elements in the literature have not been developed at present, there is no choice but to use the fiber method with *steel01* material. Deterioration is generally classified into overall and local buckling modes. Note that the deterioration of a non-prismatic element is not merely related to the cyclic deterioration of material. Hence in this study the overall buckling is considered using corotational transformation. Also, to prevent local buckling, compact sections were used (see Table 1) in which the deterioration due to local buckling was negligible. Also, the ultimate strain of the steel in the critical fibers was controlled so that it did not exceed the ultimate limit.

In modeling the non-prismatic elements of the rafters and columns, prismatic microelements with different heights were employed and six integration points were considered for each microelement. To develop the SGF model and perform gravity loading in OpenSees platform, the rafter and column members were divided into two parts and one part, respectively. Each part has its own characteristics of prismatic microelements and gravity loading, i.e., height difference between the two sections of microelements (Δh_0), length of microelements (l_0), number of microelements (n_0), point dead load of microelements (P_{D0}) and point snow load of microelements (P_{S0}), which their values are presented in Table 4. It should be noted that in the prismatic area of the rafters,

Table 4
Specifications of prismatic microelements.

	Part	Model A	Model B	Model C	Model D
Δh_0 (m)	I	0.02	0.02	0.02	0.02
	II	0.02	0.02	0.02	0.02
	III	–	–	–	–
l_0 (m)	I	0.24	0.34	0.10	0.20
	II	0.10	0.08	0.24	0.24
	III	0.25	0.20	0.60	0.60
n_0	I	2 × 25	2 × 35	2 × 60	2 × 60
	II	2 × 20	2 × 25	2 × 25	2 × 25
	III	2 × 33	2 × 41	2 × 41	2 × 41
P_{D0} (kgf)	I	86.4	122.4	36.0	72.0
	II	36.0	28.8	86.4	86.4
	III	90.0	72.0	216.0	216.0
P_{S0} (kgf)	I	–	–	–	–
	II	58.8	47.1	141.2	141.2
	III	147.1	117.7	353.0	353.0

microelements with a length of $2.5l_{0,\mathrm{II}}$ were used. Also, dead loads on the roofs and walls (i.e., rafters and columns) and snow loads only on the roofs (i.e., rafters) were applied concentratedly to each node according to the loading area. For a better understanding, the schematic view of Model D with non-prismatic elements and uniform distribution of gravity loads (initial model) is shown in Fig. 3(a) and with prismatic microelements and concentrated gravity loads (final model) in Fig. 3(b). Also, Fig. 3(c) illustrates the deformations created in model D under gravity loads. As shown in Fig. 3(c), the SGF model developed in OpenSees, in addition to considering drifts of the member ends ($\boldsymbol{\Delta}$), the local deformation relative to the member chord between the end nodes ($\boldsymbol{\delta}$) is also incorporated, where the rafter has double curvature and the column has single curvature.

3.2. Infrastructure (footing and soil)

A great body of research has been devoted to developing analytical models for SSI. Such studies may be classified into three general types, which are the finite-element methods, macro model formulations, and Winkler-based methods [53–57]. Among the mentioned analytical models, the Winkler-based methods have drawn the particular attention of scholars for their easy usability and high computational efficiency. In the present study, the modified beam on the nonlinear Winkler foundation (BNWF) model adjusted by Raychowdhury [58] was employed to incorporate the SSI effects, and for the first time, this method was developed in the OpenSees platform for the SGFs, shown in Fig. 4. The accuracy of this modeling is good in simulating nonlinear SSI with 2D problems.

As Fig. 4(a) indicates, the footing is considered as an elastic beam element in the BNWF model and the SSI is modeled with a limited number of springs. Three zero-length spring types are in this model. In the first type, in order to model the vertical (uplift and settlement) resistance of the footing, springs in a vertical array are determined with the *QzSimple2* material (*q-z* spring). The passive resistance of the soil in front of the footing is simulated by the second type, in which the *PxSimple1* material is considered for the springs (*p-x* spring). Finally, *TxSimple1* material is adopted for the springs in dealing with the sliding resistance of the soil underneath the footing (*t-x* spring).

The constitutive model of the zero-length element used in the BNWF method is illustrated in Fig. 4(b). As observed, it is comprised of three components. A drag and a closure spring are contained in component 1,

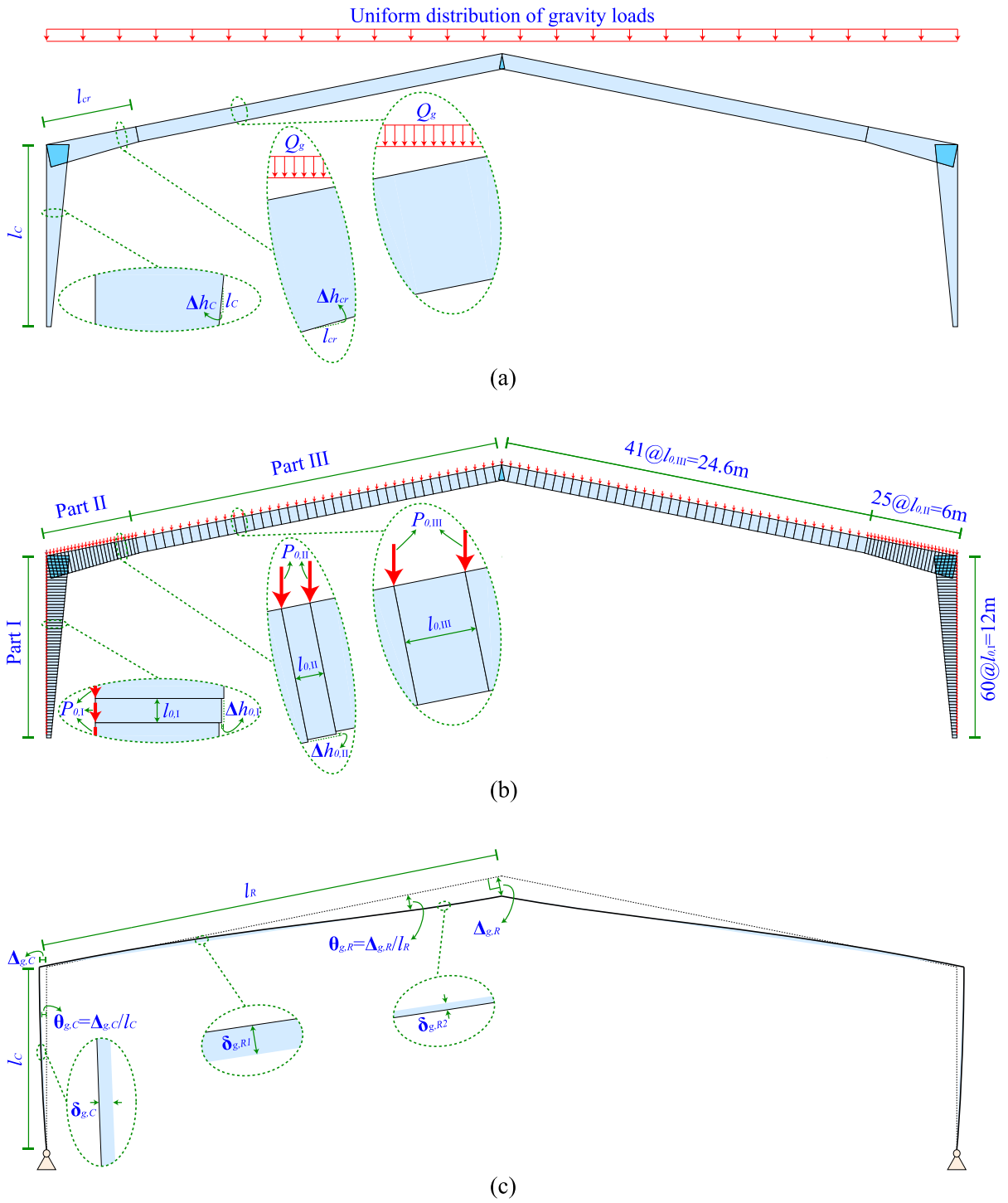

Fig. 3. Schematic representation of model D: (a) initial model, (b) final model developed in OpenSees and (c) deformations created under gravity loads.

a spring with plastic behavior in component 2, and a spring with elastic behavior connected to a damper parallelly in component 3 in order to simulate the far-field soil domain. The supporting soil medium includes (a) a near-field domain adjacent to the footing where the geometrical, as well as material non-linearity, is wholly incorporated because of SSI and (b) a far-field domain that is far enough from the footing with negligible impact of SSI non-linearity. In short, the *QzSimple2*, *PxSimple1* and *TxSimple1* material models are in fact sets of springs in series representing the far-field and near-field behavior of the soil-structure systems. Hysteretic behavior of the *QzSimple2*, *PxSimple1* and *TxSimple1* material models is shown in Fig. 4(c).

The stiffness intensity distribution along the length of the BNWF model depends on the type of structural support. In conventional buildings, which usually have fixed supports, to achieve the given rotational stiffness of the footing, the non-uniform stiffness intensity is distributed along the length of the BNWF model. Based on the recommendations of Harden and et al. [59] and ATC-40 [60], the ratio of the stiffness intensity at the end regions of the footing to that of the mid region should be larger than 1 (i.e., $R_k = k_{end} / k_{mid} > 1$). In this case, all modes of the footing movement (sliding, settling and rocking) are active under earthquake loading. Fig. 5(a) shows the BNWF mesh discretization with variable stiffness intensity for conventional buildings with

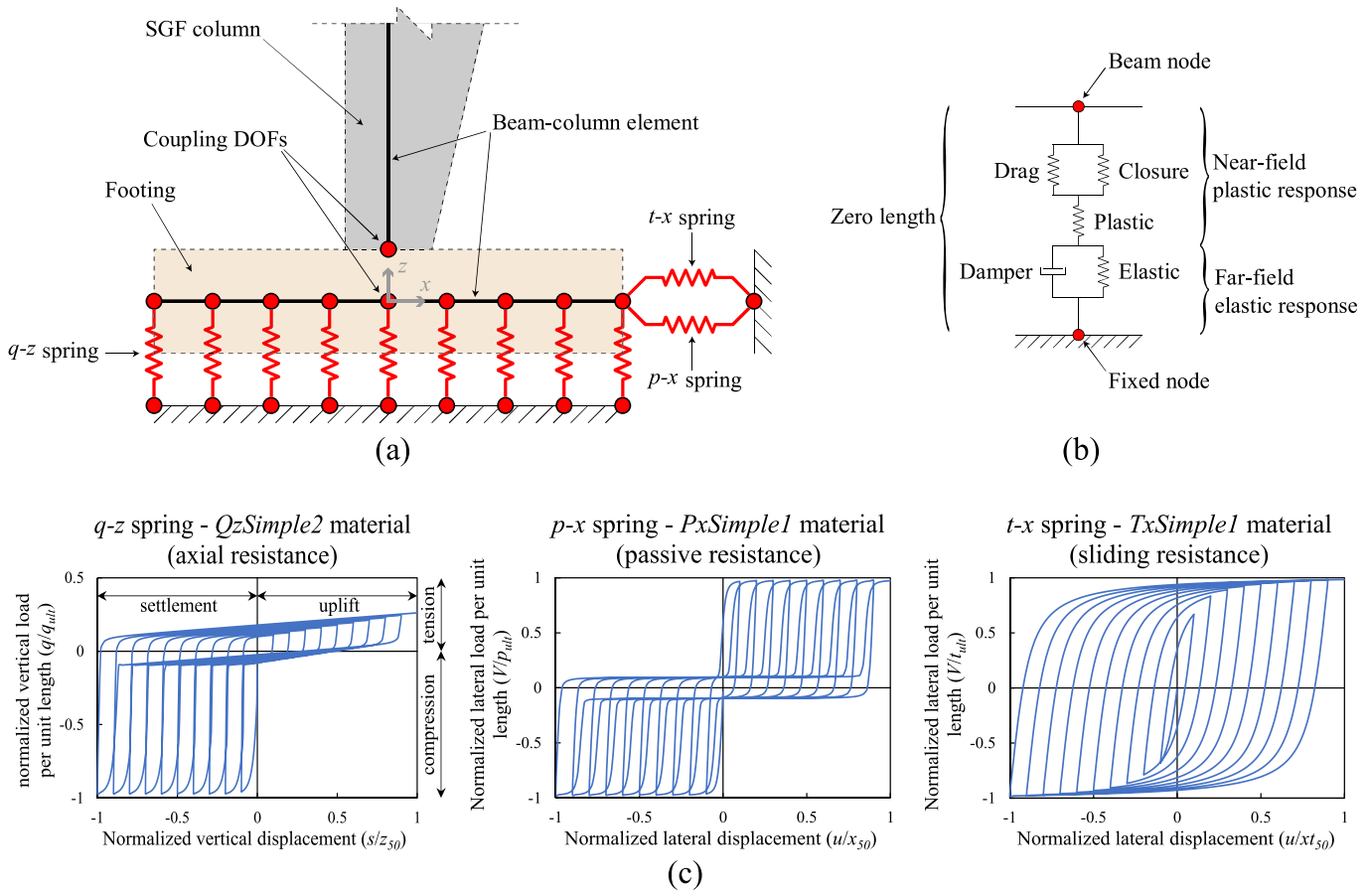

Fig. 4. BNWF method developed in OpenSees for SGFs: (a) schematic representation of BNWF model, (b) constitutive model of the zero-length element and (c) hysteretic behavior of material models.

fixed supports. On the other hand, in SGFs that usually have hinge supports, given the lack of rocking of the footings (transitional performance of the footings), the rotational stiffness of soil springs should be ignored and the uniform stiffness intensity is distributed along the length of the BNWF model. In this case, the transition modes of the footing movement (sliding, settling) are active under earthquake loading, but the rocking mode is inactive. Fig. 5(b) shows the BNWF mesh discretization with uniform stiffness intensity developed for SGFs with hinge supports. The BNWF mesh parameters for the studied SGFs are presented in Table 5.

Here, an attempt is made to briefly describe the general hysterical behavior of these material models and their calibration. As mentioned by Bolanger [61], *QzSimple2* material applied to vertical springs has an asymmetric hysterical behavior under compression and tension. In the elastic portion, the instantaneous load q is assumed to be linearly proportional with the instantaneous displacement z through the initial elastic (tangent) stiffness K_{in}, as expressed in Eq. (1):

$$q = K_{in} z \tag{1}$$

The range of the elastic portion is defined by Eq. (2):

$$q_0 = C_r q_{ult} \tag{2}$$

where q_0 is the load at the yield point, C_r is the parameter controlling the range of the elastic portion, and q_{ult} is the ultimate load.

In the nonlinear (post-yield) portion, the backbone curve is described by Eq. (3):

$$q = q_{ult} - (q_{ult} - q_0)\left[\frac{c z_{50}}{c z_{50} + |z^p - z_0^p|}\right]^n \tag{3}$$

where z_{50} is the displacement at which 50% of the ultimate load is mobilized, z_0^p is the displacement at the yield point, z^p is the displacement at any point in the post-yield portion, and c and n are the constitutive parameters controlling the shape of the post-yield portion of the backbone curve. The expressions governing both *PxSimple1* and *TxSimple1* are quite similar to Eqs. (1)–(3), with variations in the constants n, c and C_r, which control the general shape of the curve.

It is obvious from Eqs. (1)–(3) that response of nonlinear spring elements is controlled by q_{ult} and z_{50} for a particular type of soil, where z_{50} can be correlated with initial stiffness and strength parameters, as expressed in Eq. (4):

$$z_{50} = F_K \frac{q_{ult}}{K_{in}} \tag{4}$$

where F_K is a calibration factor determined for a given soil type by the results of several shallow foundation tests [58].

In the present study, the bearing capacity of the footing is determined using the equations proposed by Terzaghi [62], as follows:

$$q_{ult} = cN_c F_{cs} F_{cd} F_{ci} + \gamma D_f N_q F_{qs} F_{qd} F_{qi} + 0.5\gamma B N_\gamma F_{\gamma s} F_{\gamma d} F_{\gamma i} \tag{5}$$

where the q_{ult} is the ultimate vertical bearing capacity per unit area of footing, c the cohesion, γ parameter denotes the unit weight of soil; c represents the soil cohesion; D_f and B indicate the depth of embedment and the width of footing, respectively; and (F_{cs}, F_{qs}, F_{gs}), (F_{cd}, F_{qd}, F_{gd}), and (F_{ci}, F_{qi}, F_{gi}) parameters denote the shape, depth, and inclination factors, respectively, defined by Meyerhof [63]. Bearing capacity factors, N_γ, N_c and N_q are calculated by [63–65], respectively. These are as follows:

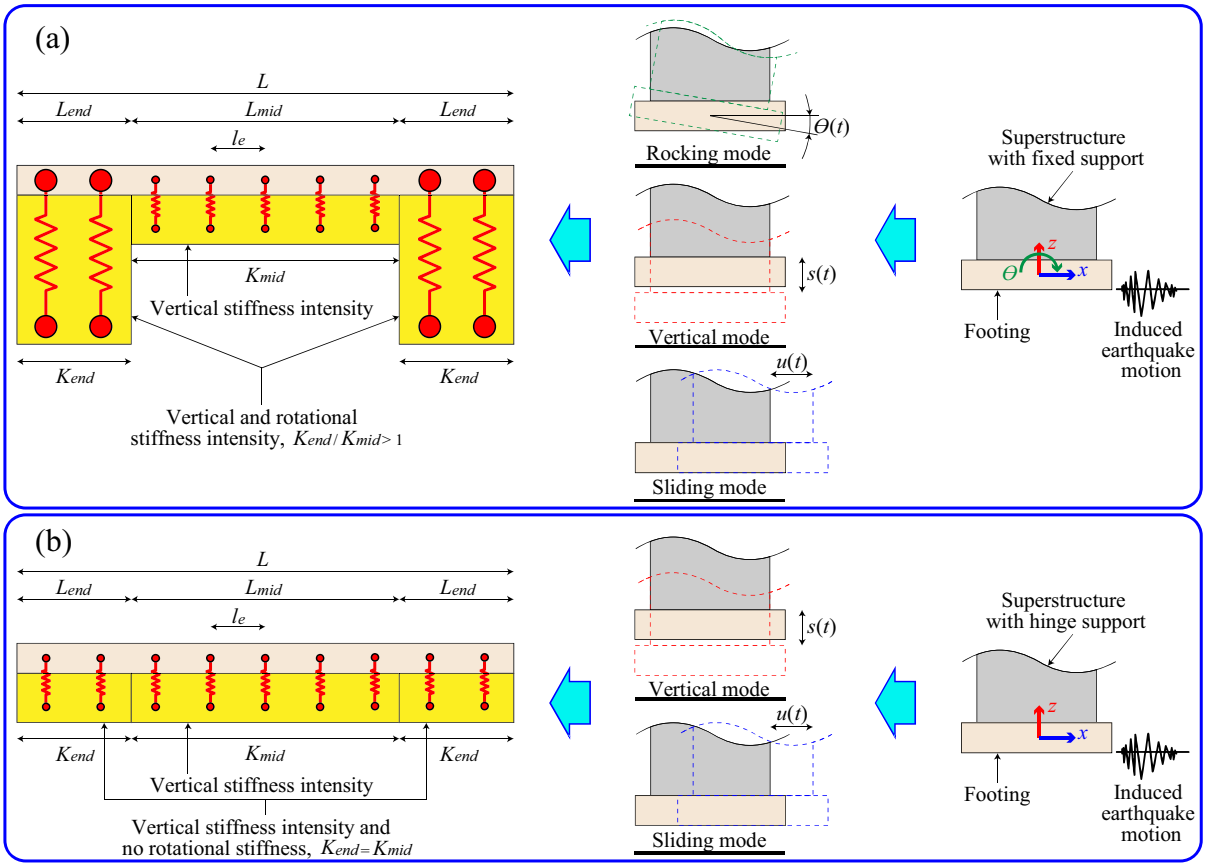

Fig. 5. BNWF mesh discretization: (a) variable stiffness intensity for conventional buildings with fixed supports [59,60] and (b) uniform stiffness intensity developed for SGFs with hinge supports.

Table 5
BNWF mesh parameters for the studied SGFs.

Parameters	Value
Stiffness intensity ratio, $R_k = K_{end} / K_{mid}$	1
End length ratio, $R_e = L_{end} / L$	–
Spring spacing, $S_e = l_e / L$	2%

$$N_\gamma = (N_q - 1)tan(1.4\phi) \tag{6}$$

$$N_q = tan^2\left(45^o + \frac{\phi}{2}\right)e^{\pi tan\phi} \tag{7}$$

$$N_c = (N_q - 1)cot\phi \tag{8}$$

where ϕ is the effective friction angle.

The vertical and lateral stiffness of the footing (K_v and K_h) are calculated by Gazetas equations [66]:

$$K_v = \frac{GL}{1-\nu}\left[0.73 + 1.54\left(\frac{B}{L}\right)^{0.75}\right] \tag{9}$$

$$K_h = \frac{GL}{2-\nu}\left[2 + 2.5\left(\frac{B}{L}\right)^{0.85}\right] \tag{10}$$

where G and ν are the shear modulus and Poisson's ratio of soil, and B and L are the width and length of the footing.

In the nonlinear portion of the backbone curves, the post-yield tangent stiffness, k_p, of the footing is calculated from Eq. (11) [58]:

$$k_p = \frac{n(q_{ult} - q_0)(cz_{50})^n}{(cz_{50} - z_0 + z)^{n+1}} \tag{11}$$

By incorporating the homogeneous backfill against the footing, for *p-x* spring element (*PxSimple1* material), the passive resistance, p_{ult}, acting on the front side of the embedded footing can be calculated using a linearly varying pressure distribution as follows [58]:

$$p_{ult} = 0.5\gamma D_f^2 K_p \tag{12}$$

where K_p is the passive earth pressure coefficient.

Using the classical Mohr-Coulomb failure criteria and ignoring friction on the sides and front of the footing, the total sliding (frictional) resistance, t_{ult}, for *t-x* spring element (*TzSimple1* material) can be determined as the shear strength between the soil and the footing by Eq. (13) [58]:

$$t_{ult} = W_g tan\delta + A_b c \tag{13}$$

where W_g is a vertical force applied to the footing, δ is the friction angle between soil and footing ($1/3\phi < \delta < 2/3\phi$), and A_b is the footing area ($L \times B$).

Further information about the BNWF model can be found in Ref. [58]. According to Eqs. (1)–(13), parameters of *q-z*, *p-x*, and *t-x* springs (*QzSimple2*, *PxSimple1* and *TxSimple1* materials, respectively) are determined and are presented in Table 6. As mentioned, the ultimate capacities of the *q-z*, *p-x* and *t-x* springs are respectively indicated by q_{ult}, p_{ult}, and t_{ult}. In addition, z_{50}, x_{50}, and xt_{50} stand for the displacement of springs in both vertical and lateral directions with 50% of the load capacity in the respective directions.

Table 6
Parameters of q-z, p-x, and t-x springs.

Model Name	*q-z* spring		*p-x* spring		*t-x* spring	
	q_{ult} (kN)	z_{50} (mm)	p_{ult} (kN)	x_{50} (mm)	t_{ult} (kN)	xt_{50} (mm)
A	54	18.01	29	0.10	63	0.78
B	54	18.01	29	0.10	77	0.97
C	1008	118.02	454	0.53	226	1.00
D	373	62.82	176	0.29	218	1.36

4. Validation of the studied models

Since there was no similar laboratory reference for the nonlinear models developed in OpenSees software, they were compared in three steps by modal, pushover, and nonlinear time-history analyses with the results of SAP2000 [67], a software tool that has been shown to provide reliable nonlinear structural response estimates. Accordingly, it was necessary to identify the characteristics of the materials, *sec*tions, and nonlinear elements for the models developed in SAP2000 in accordance with those in the OpenSees. The results obtained by both pieces of software were compared for the mentioned three types of analysis. As mentioned before, validation of models located on flexible substrates by the BNWF method is presented in Raychowdhury's report in Ref. [58]. As a result, in this section, only validation of the nonlinear behavior of models located on the rigid substrate is provided.

4.1. Modal analysis

Validation of models by the modal analysis was gone through with the aim of comparing the dynamic properties such as the first-mode period (fundamental period) of the structure in the OpenSees and SAP2000 software. The fundamental periods of the models located on rigid substrate in the modal analysis by the mentioned software are represented in Table 7. To compare the mentioned periods on rigid and flexible substrates, the fundamental periods of the models implemented on the flexible substrate in association with the modal analysis were determined in OpenSees software, as given in Table 7.

As observed in Table 7, the percentage of error between the fundamental periods in both pieces of software is negligible, proving the accurate modeling of SGFs in the linear region. Also, it was observed that consideration of SSI leads to a slight increase in the fundamental period of Models A, B, C, and D, equal to 0.22, 0.13, 0.32, and 0.15%, respectively.

4.2. Pushover analysis

The aim of the nonlinear static (pushover) analysis was the comparison of the nonlinear behaviors of the structure in the OpenSees and SAP2000 software. Fig. 6 illustrates diagrams for the drift to the base shear (pushover curves) derived from the pushover analysis for model D as a sample in both pieces of software. Prior to conducting any static or dynamic analysis under earthquake load, it is required to carry out the static analysis under gravity loads. Due to the greater criticality of balanced snow load than its unbalanced counterpart, the balanced snow load was used in conjunction with dead load in the gravity analysis. Of note, the target drift was identified with the help of FEMA 356.

Table 7
Fundamental period of the studied models.

Model Name	Base	OpenSees (sec)	SAP2000 (sec)	Error (%)
A	Fixed	0.896	0.884	1.35
B	Fixed	1.533	1.513	1.32
C	Fixed	0.626	0.618	1.29
D	Fixed	1.312	1.298	1.08
A	Flexible	0.898	–	–
B	Flexible	1.535	–	–
C	Flexible	0.628	–	–
D	Flexible	1.314	–	–

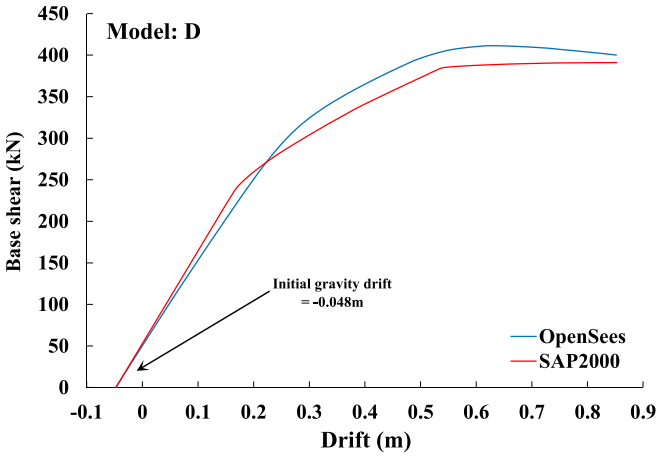

Fig. 6. Pushover curve for model D.

According to the pushover curves of Fig. 6, there is a slight difference in the linear region, which indicates accurate modeling of the linear region in both pieces of software, supporting the validation results of the modal analysis for this region. Furthermore, almost similar behaviors are also observed in the nonlinear region, indicating the acceptability of the results. As mentioned in the literature, SGFs do not have significant ductility due to their low degree of indeterminacy, and with the formation of a small number of plastic hinges, instability occurs in this type of structure, as can be clearly seen in Fig. 6. Of note, due to the specific geometrical characteristics of SGFs (sloping beams), gravity loads would induce an initial negative drift in the shoulder. In addition, the existence of hinge supports would intensify the mentioned negative drift, as can be clearly seen in Fig. 6.

4.3. Nonlinear time-history analysis

Validating the models through nonlinear time-history analysis was carried out with the aim of comparing the dynamic properties as well as the nonlinear behaviors of the structure in SAP2000 and OpenSees software. In Fig. 7, results for the nonlinear time-history analysis for model D using the Imperial Valley-06 earthquake record at the Bonds Corner station with a peak ground acceleration (PGA) of 0.78 g are provided in the form of horizontal displacement time-history curves corresponding to the shoulder node using both pieces of software. Since the analysis presented in the present paper consists of a large number of nonlinear time-history analyses under a set of ground motion records, the most important step of the validation belongs to this part.

As can be seen in Fig. 7, the dynamic properties and the nonlinear behavior of the structure are almost identical with a slight difference in both pieces of software, which indicates the correct coding and accurate modeling in the OpenSees platform. As mentioned earlier, SFGs experience a static displacement in the initial state due to gravity loads. After incorporating the ground motion records, the absolute maximum displacement for SFGs involves initial static displacement resulting from the gravity loads plus maximum dynamic displacement resulting from the ground motion records.

5. Earthquake records selection

Since the dynamic response of a system is highly dependent on the earthquake records, an appropriate number of records must be selected to cover the response range of the structure. For this purpose, FEMA P695 [68] has introduced a set including 22 pairs of far-field records and

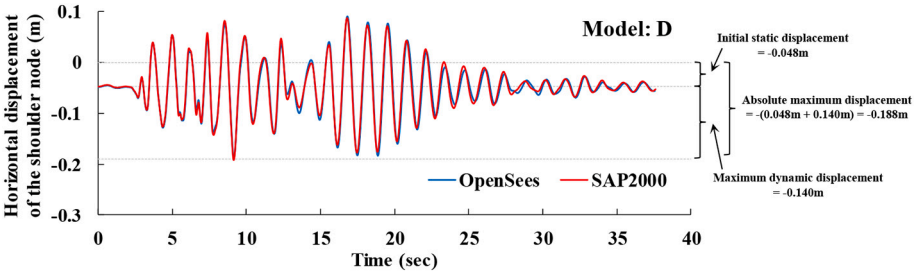

Fig. 7. Horizontal displacement time-history curve corresponding to the shoulder node for model D.

28 pairs of near-field records. With reference to the 28 pairs of near-field records, 14 pairs of records are identified as pulse-like. This set covers a wide range of moment magnitude (M_W) between 6.5 and 7.9 and the closest distance from the recording site to the ruptured area (R_{rup}) is up to about 25 km. Criteria such as the source magnitude, source type, site conditions, source-to-site distance, the intensity of a seismic event, and the quality and reliability of the recording process are included in this selection. More information on this set of records and their selection is available in Appendix A of FEMA P695. Furthermore, according to Shome and Cornell [69], the use of 10 to 20 records often leads to acceptable accuracy in damage demand estimation. Accordingly, in this study, 20 records in FEMA P695 were selected from the PEER-NGA database [70] with the tectonic characteristics of Class D soil (similar to the background soil assumed). Out of every record, only one horizontal component with more PGA was used in conjunction with the vertical component. The details of the selected records are given in Table 8. Also, their elastic response spectrum was created by Seismosignal software [71].

6. IDA analysis

6.1. Overview

As described in Section 4.3, IDA analysis includes a large number of nonlinear time-history analyses under a set of ground motion records. These records are scaled in such a way that they can cover the range of linear and nonlinear behaviors as well as the collapse of a structure. The scale factor of records is defined as a multiplication of the intensity measure (IM) from a very low level to a high level at which the collapse of the structure occurs. Also, the damage measure (DM) is recorded in each analysis. The diagram of DM against IM values on the basis of which the ground motion records are scaled is called the IDA curve.

6.2. IM and DM selection

In the IDA analysis, an important part is selecting the proper IM and DM. Selecting an appropriate IM reduces the statistical dispersion of the IDA analysis data. The selection of the appropriate DM should be based on the expected performance of the structure as well as its dominant failure mechanism. In the present paper, the 5% damped first-mode spectral acceleration ($Sa(T_1,5\%)$) and the absolute maximum drift angle (Θ_{max}) were selected as IM and DM, respectively.

6.3. Performance levels

One of the methods of determining the structure performance corresponding to the specified level of damage and a given limit of the structure capacity before collapse is employing a criterion that shows the limit state of its behavior; when the behavior of a structure crosses the criterion, a limit state occurs and the structure enters a new region. In the present research, based on FEMA 356, three performance levels (i.e., limit states) of Immediate Occupancy (IO), Life Safety (LS) and Collapse Prevention (CP) with the Θ_{max} values of 0.7, 2.5, and 5% were selected, respectively.

6.4. Multi-record IDA curves

Multi-record IDA curves well demonstrate the structural behavior from the linear region to the collapse of a structure for a set of records selected based on the desired properties. The multi-record and summarized IDA curves for the studied SGFs are shown in Fig. 8. As described above, given the particular geometrical characteristic of SFGs,

Table 8
Selected records for IDA analysis.

No.	Event	Station	M_w	R_{rup} (km)	V_{S30} (m/s)	$PGA_{V/H,MAX}$	Record set	Pulse
1	Duzce Turkey	Bolu	7.14	12.04	293.57	0.248	Far-field	No
2	Loma Prieta	Capitola	6.93	15.23	288.62	1.087	Far-field	No
3	Chi-Chi Taiwan	CHY101	7.62	9.94	258.89	0.417	Far-field	No
4	Landers	Coolwater	7.28	19.74	352.98	0.424	Far-field	No
5	Imperial Valley-06	Delta	6.53	22.03	242.05	0.407	Far-field	No
6	Loma Prieta	Gilroy Array #3	6.93	12.82	349.85	0.613	Far-field	No
7	Superstition Hills	El Centro Imp. Co. Cent	6.54	18.20	192.05	0.358	Far-field	No
8	Northridge-01	Canyon-W Lost Cany	6.69	12.44	325.6	0.641	Far-field	No
9	Northridge-01	Beverly Hills-Mulhol	6.69	17.15	355.81	0.667	Far-field	No
10	Kobe Japan	Shin-Osaka	6.90	19.15	256.00	0.289	Far-field	No
11	San Fernando	LA-Hollywood Stor FF	6.61	22.77	316.46	0.730	Far-field	No
12	Northridge-01	Rinaldi Receiving Sta	6.69	6.50	282.25	1.099	Near-field	Yes
13	Duzce Turkey	Duzce	7.14	6.58	281.86	0.671	Near-field	Yes
14	Imperial Valley-06	El Centro Array #6	6.53	1.35	203.22	4.167	Near-field	Yes
15	Imperial Valley-06	El Centro Array #7	6.53	0.56	210.51	1.235	Near-field	Yes
16	Erzican Turkey	Erzincan	6.69	4.38	352.05	0.474	Near-field	Yes
17	Chi-Chi Taiwan	TCU065	7.62	0.57	305.85	0.333	Near-field	Yes
18	Imperial Valley-06	Bonds Corner	6.53	2.66	223.03	0.685	Near-field	No
19	Imperial Valley-06	Chihuahua	6.53	7.29	242.05	0.885	Near-field	No
20	Kocaeli Turkey	Yarimca	7.51	4.83	297.00	0.752	Near-field	No

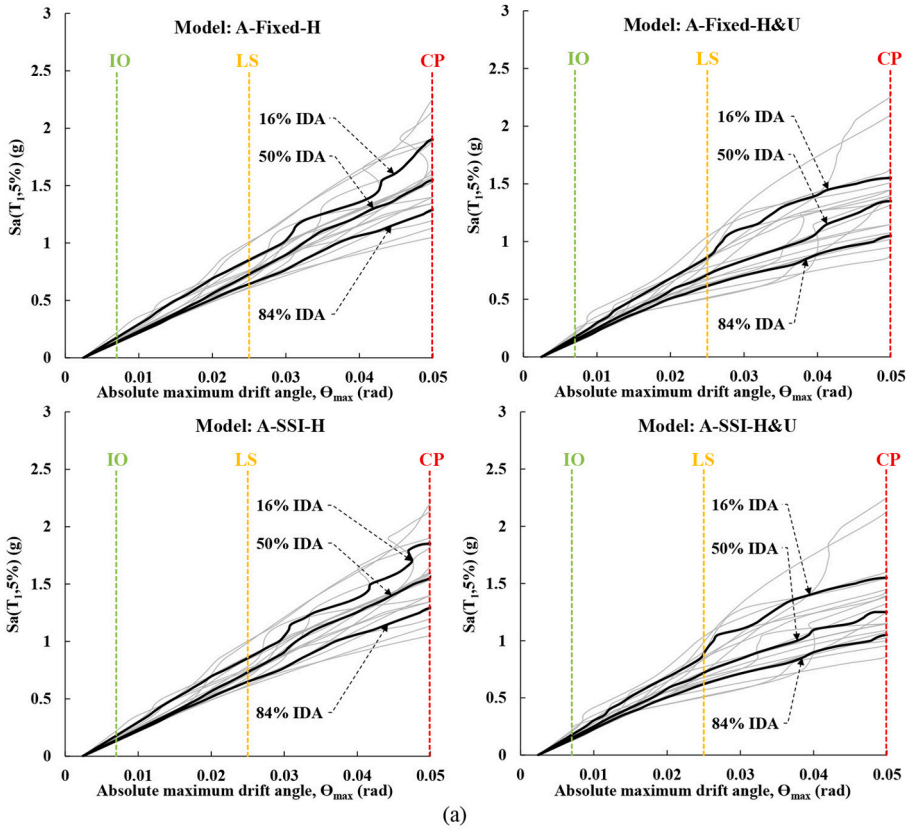

Fig. 8. Multi-record and summarized IDA curves for (a) model A, (b) model B, (c) model C and (d) model D.

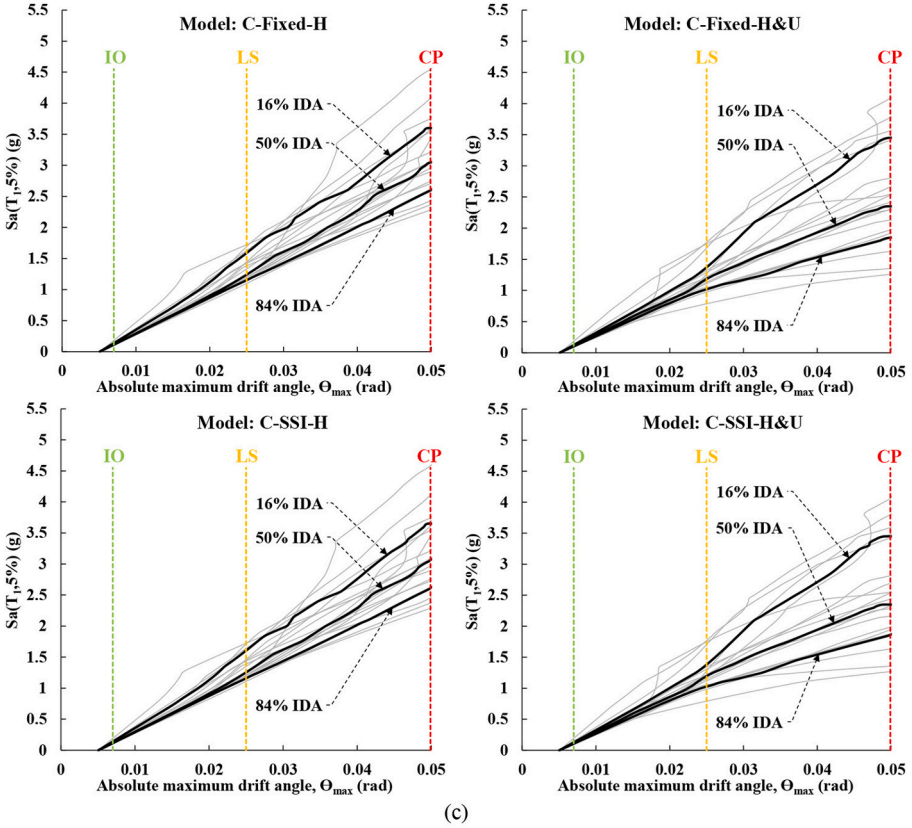

(c)

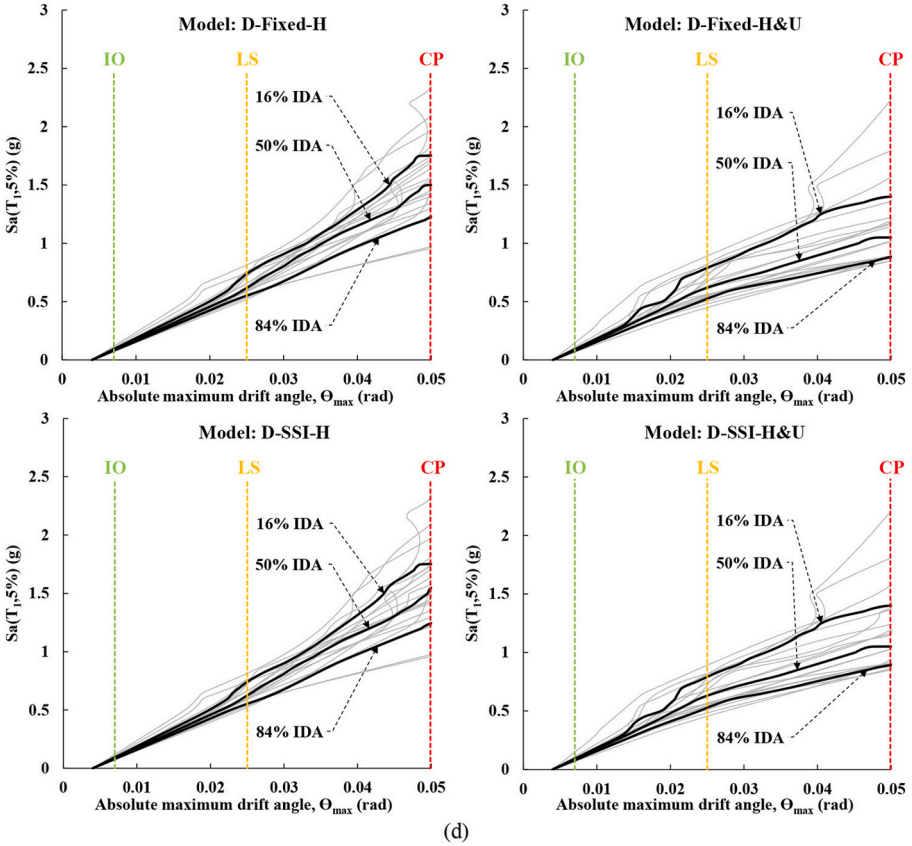

(d)

Fig. 8. (*continued*).

gravity loads create an initial negative Θ_{max} in the shoulder, which intensifies due to the existence of hinge supports and appears positive in the IDA curves due to its absolute value. This can clearly be observed in Fig. 8.

As can be seen in Fig. 8, considering the combined effect of the horizontal and vertical components (shown in Figs. with H&U) increases the stiffness changes in the nonlinear region of the structure and is absolutely influential on data dispersion and demand sensitivity, as a result of which the linear region has been reduced relative to incorporating the horizontal component alone (shown in Figs. with H). In addition, by considering both the horizontal and vertical components, most records bring the structure to the CP performance level at lower intensities and the structure exhibits a softening behavior, which is clearly visible in all models. Moreover, SSI has not exerted much change in the behavior of SGFs under different records compared with the rigid substrate state.

6.5. Summarized IDA curves

Multi-record IDA curves indicate a large difference between one record and another. Hence, they should be summarized to reduce data dispersion. A method of summarization is the use of 16, 50 and 84% percentiles. Summarized IDA curves are also called structural dynamic capacity (tolerable IM value for a structure or IM capacity) curves, which are mainly used to compare structures relative to each other [72].

According to Fig. 8, when the horizontal and vertical components are applied simultaneously, the obtained dynamic capacity values from the summarized IDA curves for the SGFs with various spans and heights clearly indicate different seismic performance compared to incorporating only the horizontal component. In the 50% IDA curves at the CP performance level, considering the vertical component of earthquake reduces the dynamic capacity of Models A, B, C and D by 11, 8, 22 and 28% and in the 84% IDA curves, which is used for important structures, the reduction is 18, 3, 29 and 28%, respectively, so that the amount of reduction in dynamic capacity at the LS and IO performance levels becomes less significant. Furthermore, incorporating SSI into all performance levels exerts an insignificant effect on the dynamic capacity of SGFs compared with the rigid substrate status, so that on average, with the 50% and 84% IDA curves at all performance levels, Models A, B, C and D experience 1, 0, 4 and 2% increase in the dynamic capacity, respectively. However, the effect of SSI on the dynamic capacity of SGFs is almost constant at all performance levels.

7. PSDA

7.1. Overview

PSDA is an approach to calculating the MAF (annual probability) of exceeding a specified seismic demand for a given structure at a designated site. This method integrates the IM hazard curve for the study region, which is calculated by probabilistic seismic hazard analysis (PSHA), into the results of a nonlinear dynamic analysis of the structure under the influence of a group of ground motion records. It is in fact an application of the total probability theorem as the base for the PSHA method. Using DM and IM, PSDA is expressed mathematically in Eq. (14) [73]:

$$\lambda_{DM}(y) = \int G_{DM|IM}\left(y|x\right)\left|d\lambda_{IM}(x)\right| \tag{14}$$

where $\lambda_{DM}(y)$ denotes the MAF of DM exceeding the value y (DM hazard); likewise, $\lambda_{IM}(x)$ is the IM hazard and $d\lambda_{IM}(x)$ is its differential at x. In simplistic terms, $d\lambda_{IM}(x)$ is the annual probability of observing a particular value of IM. The term $G_{DM|IM}(y|x)$, which is usually calculated using the results of nonlinear dynamic analysis under a series of ground motion records, denotes the probability of DM exceeding the value y given that IM equals x. It should be noted that the term $G_{DM|IM}(y|x)$ refers to the uncertainty of structural demand at a particular level of IM due to differences among earthquakes.

With structural capacity information, the results of PSDA (i.e., λ_{DM}) can be used to calculate the MAF of exceeding a specified limit state (e.g., the CP limit state), often referred to as an annual limit state frequency. The MAF of exceeding a specified limit state, denoted by λ_{LS}, is expressed by Eq. (15) [73]:

$$\lambda_{LS} = \int G_{LS|DM}(y).\left|d\lambda_{DM}(y)\right| \tag{15}$$

where $d\lambda_{DM}(y)$ denotes the differential of DM hazard; in effect, it is the annual probability of observing a particular value of DM. The term $G_{LS|DM}(y)$ denotes the probability of exceeding a specified limit state, given that DM equals y. The MAF of exceeding a specified limit state, by expansion Eq. (2), is reached by Eq. (16) [72]:

$$\lambda_{LS} = \int_{IM=0}^{IM=+\infty} F\left(IM^{LS}|IM\right).\left|\frac{d\lambda_{IM}}{dIM}\right|dIM \tag{16}$$

where the quantity in the absolute value is the IM hazard gradient and $F(IM^{LS}|IM)$ is the cumulative distribution function (CDF) of the IM value of a specified limit state. To calculate λ_{LS}, first, the CDF of the IM value of a specified limit state, called the fragility curve, should be obtained. Then, having the IM hazard gradient of the study region in hand, Eq. (16) can be easily calculated by the numerical integration method.

7.2. Fragility curves

In order to derive the probability of exceeding a specified limit state from the outputs of IDA analysis, diagrams called fragility curves are used. To draw these diagrams, first, the IM values corresponding to a specified limit state are arranged in descending order for all records. Then, the probability of exceeding the limit state in the structure is calculated for values less than or equal to the given IM, which is a CDF, and its diagram is plotted against IM. These curves indicate the probability of exceeding a specified limit state for each IM level, regardless of the IM hazard in the study region, provided that the IM is limited to the given level. The fitted fragility curves for the studied SGFs at the IO, LS and CP limit states are shown in Fig. 9.

Fig. 9 clearly shows the difference between fragility curves for the SGFs with different spans and heights when the horizontal and vertical components are applied, simultaneously, and when only the horizontal component is considered. As observed, at the CP performance level, considering the vertical component of earthquake in all models, especially in Models C and D (wide-span SGFs), increases the failure probability at any intensity. At the LS performance level, it is seen that considering the vertical component of earthquake in all models increases the failure probability at low intensities and vice versa. The mentioned reduction in the failure probability at high intensities may be due to the opening of SGFs by the vertical acceleration of earthquake in the downward direction (from top to bottom) and the positive horizontal displacement created in the shoulder by the horizontal acceleration of earthquake in the positive direction (from left to right). Concurrency of the two reduces the horizontal displacement in the shoulder, which due to the fact that the earthquake excitations are cyclic, the opposite occurs similarly. Otherwise, considering the vertical component could increase the horizontal displacement in the shoulder. Hence, in case the vertical component is considered, greater data dispersion is expected and consequently, the slope of the fragility curve decreases, which indicates greater uncertainty. According to the observations, at the IO performance level, the influence of incorporating the vertical component of earthquake on the failure probability is negligible in models A and B, while it cannot be overlooked in models C and D. This low failure probability at the IO performance level may be due to the initial static displacement that causes SGFs to experience this performance level at

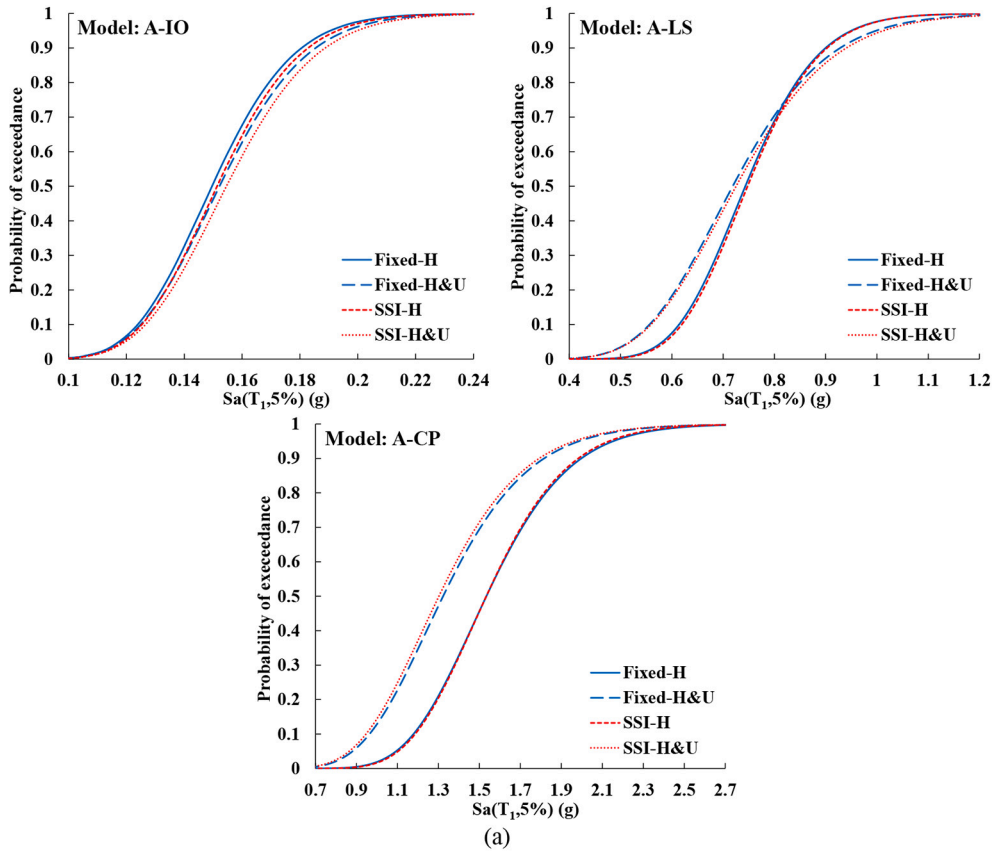

Fig. 9. Fitted fragility curves at the IO, LS and CP limit states for (a) model A, (b) model B, (c) model C and (d) model D.

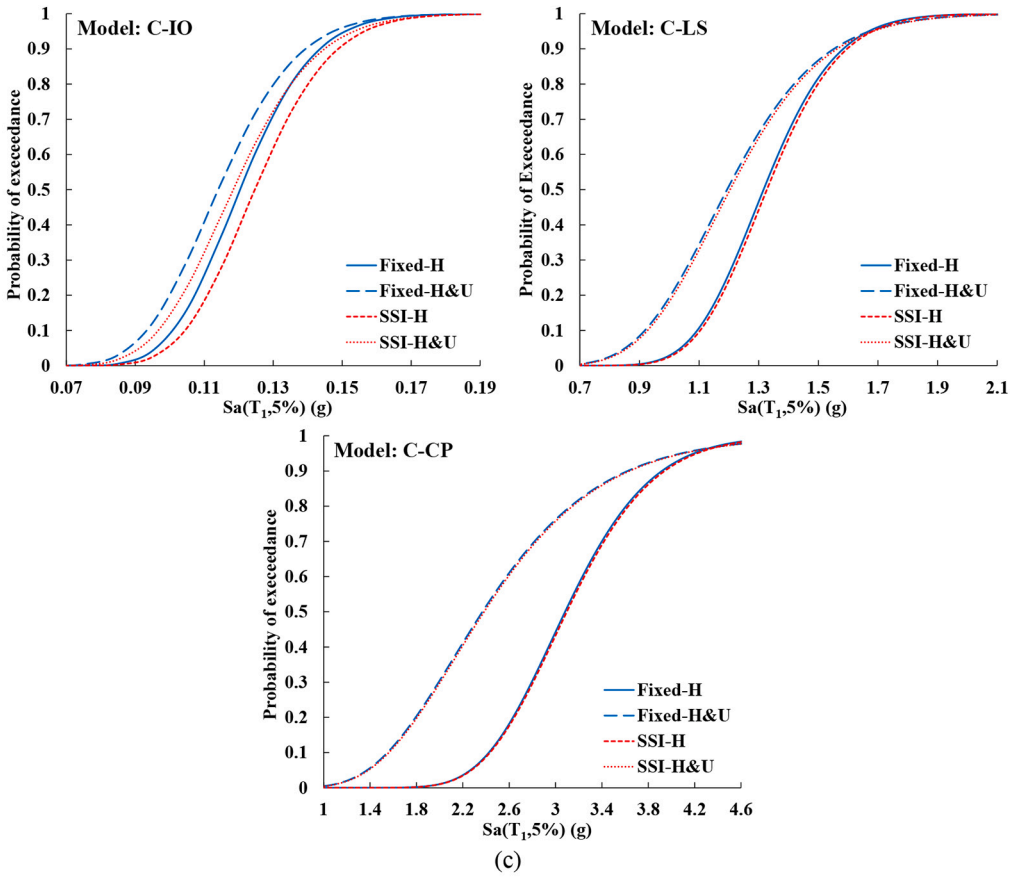

(c)

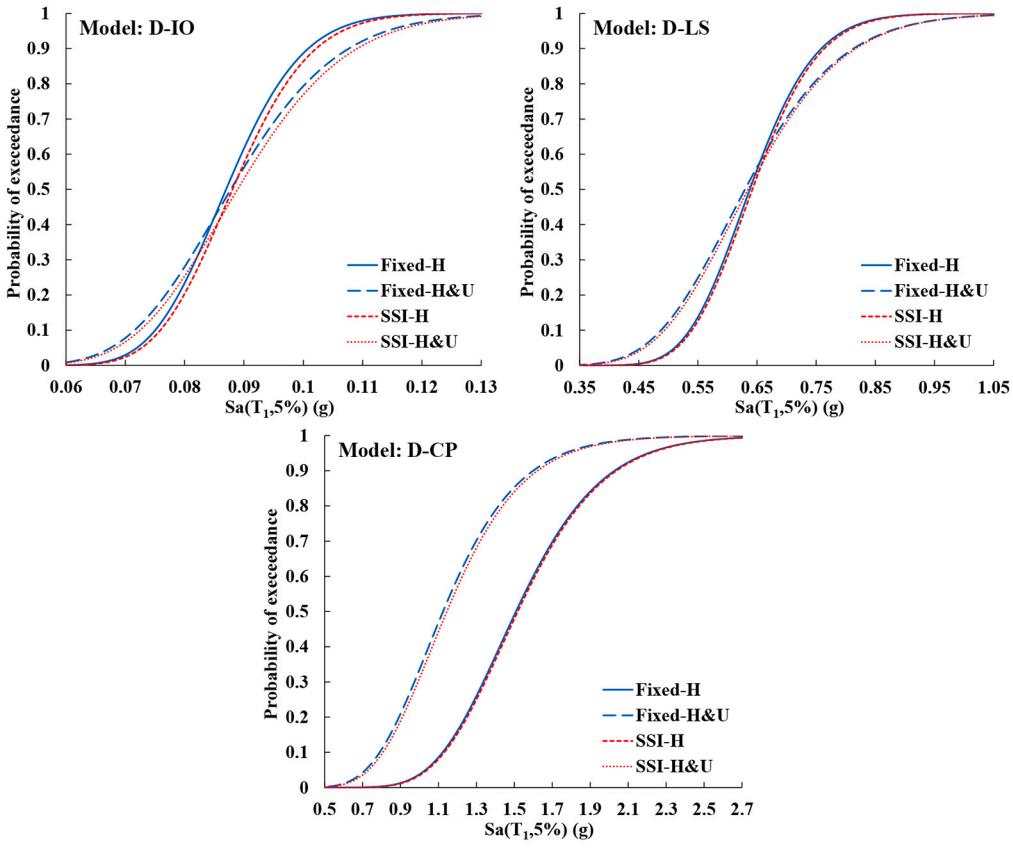

(d)

Fig. 9. (*continued*).

very low earthquake intensities, especially when they have a short span. In addition, it is seen that considering the vertical component of earthquake at all performance levels, on average, leads to enhancing the uncertainty and accelerates the damage of SGFs (inverse the slope of the fragility curve), especially when they have wide spans. Also, considering SSI at all performance levels, on average, leads to a slight reduction in the failure probability of SGFs, especially when they have wide spans. However, the effect of SSI on the failure probability of SGFs at all performance levels is almost constant.

7.3. IM hazard curves

In order to calculate the MAF of the limit states using numerical integration from Eq. (16), in addition to having fragility curves, it is necessary to determine the IM hazard gradient. However, in order to calculate the IM hazard gradient, PSHA for the study region is required. By determining the simplified uniform hazard spectra with 75-year, 475-year and 2475-year return periods ($T_{R\text{-}75}$, $T_{R\text{-}475}$ and $T_{R\text{-}2475}$, respectively) for the study region, the estimation of the IM hazard gradient is easily achievable, which is discussed in detail below. The IM hazard curve is expressed by a second-order polynomial in a log space in Eq. (17) [74]:

$$\lambda_{IM} = k_0\, exp\left(-k_1 ln IM - k_2 ln^2 IM\right) \tag{17}$$

with k_1, $k_2 > 0$ and $k_0 \geqslant 0$, the latter indicating the (local) hazard curvature. The unknown parameters k_0, k_1 and k_2 need to be calculated in order to determine the IM hazard curve. To this end, the following steps need to be taken. First, the simplified uniform hazard spectra with $T_{R\text{-}75}$, $T_{R\text{-}475}$ and $T_{R\text{-}2475}$ for Class D soil are obtained using Ref. [75] for 22 different regions of Tehran (see Fig. 10). Second, the average of the mentioned spectra is calculated for 22 different regions of Tehran (see Fig. 10). Third, the spectral accelerations corresponding to the fundamental period of the studied models are determined using the average of simplified uniform hazard spectra with $T_{R\text{-}75}$, $T_{R\text{-}475}$ and $T_{R\text{-}2475}$ (Sa_{75}, Sa_{475} and Sa_{2475}, respectively) for 22 different regions of Tehran (see Table 9). Fourth, λ_{IM} is considered equal to the inverse of $T_{R\text{-}75}$, $T_{R\text{-}475}$ and $T_{R\text{-}2475}$, and IM is equal to the Sa_{75}, Sa_{475} and Sa_{2475}. Keeping the above in mind, Eq. (4) can be rewritten into the following form:

$$\begin{cases} \dfrac{1}{T_{R-75}} = k_0\, exp\left(-k_1 ln Sa_{75} - k_2 ln^2 Sa_{75}\right) \\ \dfrac{1}{T_{R-475}} = k_0\, exp\left(-k_1 ln Sa_{475} - k_2 ln^2 Sa_{475}\right) \\ \dfrac{1}{T_{R-2475}} = k_0\, exp\left(-k_1 ln Sa_{2475} - k_2 ln^2 Sa_{2475}\right) \end{cases} \tag{18}$$

By solving the three-equation and three-unknown system in Eq. (18), the unknown parameters k_0, k_1 and k_2 are calculated (see Table 9).

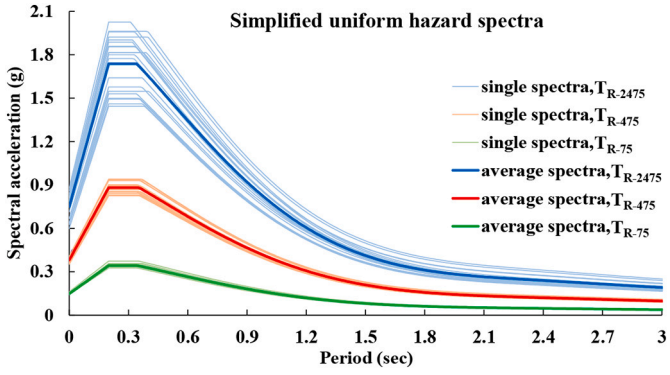

Fig. 10. Single and average simplified uniform hazard spectra with $T_{R\text{-}2475}$ and $T_{R\text{-}475}$ and $T_{R\text{-}75}$ for 22 different regions of Tehran.

Table 9
IM hazard curve parameters.

Parameters	Model A	Model B	Model C	Model D
Sa_{2475}	0.916	0.396	1.319	0.513
Sa_{475}	0.463	0.200	0.670	0.259
Sa_{75}	0.180	0.078	0.261	0.101
k_0 (1.E-05)	32.058	2.875	82.000	6.250
k_1	2.667	3.112	2.474	2.988
k_2 (1.E-01)	2.864	2.777	2.973	2.834

Having the values of k_0, k_1 and k_2, the IM hazard curve and the IM hazard gradient for the studied SFGs are determined. Due to the almost identical fundamental periods of the models located on rigid and flexible substrates, the IM risk curve and the IM risk gradient are both quite similar.

7.4. MAF of the limit states

Using the fragility curves and the IM hazard gradient of the study region given in Sections 7.2 and 7.3, respectively, numerical integration from Eq. (16) was performed. The MAF values for the studied SGFs at the IO, LS and CP limit states are shown in Fig. 11. These values can be used as a criterion for measuring the reliability of the structures under study in comparison with other structural systems or they can be employed in the codes related to the design of such structures.

As clearly indicated in Fig. 11, the MAF values for the SGFs with various spans and heights when the horizontal and vertical components are applied to them, simultaneously, are different from the case of incorporating only the horizontal component. Considering the vertical component of earthquake for Models A, B, C and D increases the MAF value at the CP performance level by 58, 18, 186 and 126%, respectively; at the LS performance level by 27, 20, 60 and 33%, respectively; and at the IO performance level by −6, −13, 15 and 24%, respectively. Also, considering SSI at all performance levels has a negligible effect on the MAF of SGFs and, on average, for Models A, B, C and D, 1, 0, 3 and 3% reduction is observed, respectively. In addition, under similar conditions, on average at all performance levels, Models A and C (short-period SGFs) have higher MAF than Models B and D (long-period SGFs). This is due to the fact that in the IM hazard curves, the MAF values decrease with increasing the fundamental period of SGFs.

7.5. PSDA curves

The output of the PSDA is the curves that estimate the MAF for different values of DM, each of which can be considered as a limit state. Hence, the PSDA curves were calculated using the numerical integration from Eq. (16) by considering different values of DM as the limit states, the results of which are shown in Fig. 12. These curves can be used in the performance-based design for this type of structure to determine the design earthquakes with return periods commensurate with a given DM.

As can be seen in Fig. 12 and mentioned above, considering the vertical component of earthquake significantly increases the MAF of SGFs, especially when they have wide spans, and it becomes less with decreasing Θ_{max}. In other words, when the strongest earthquake is expected to occur, the effect of the vertical component of earthquake increases sharply, and on the other hand, when low-intensity earthquakes are expected, its influence decreases. Also, incorporation of SSI in all Θ_{max}'s has a negligible effect on the MAF of SGFs and, on average, slightly reduces it, especially when they have wide spans. However, the effect of SSI on the MAF of SGFs is almost constant at all Θ_{max}'s. Moreover, as described in Section 7.4, under similar conditions, on average in all Θ_{max}'s, Models A and C (short-period SGFs) have higher MAF than Models B and D (long-period SGFs), because, in the IM hazard curves, the MAF values decrease with increasing the fundamental period of SGFs.

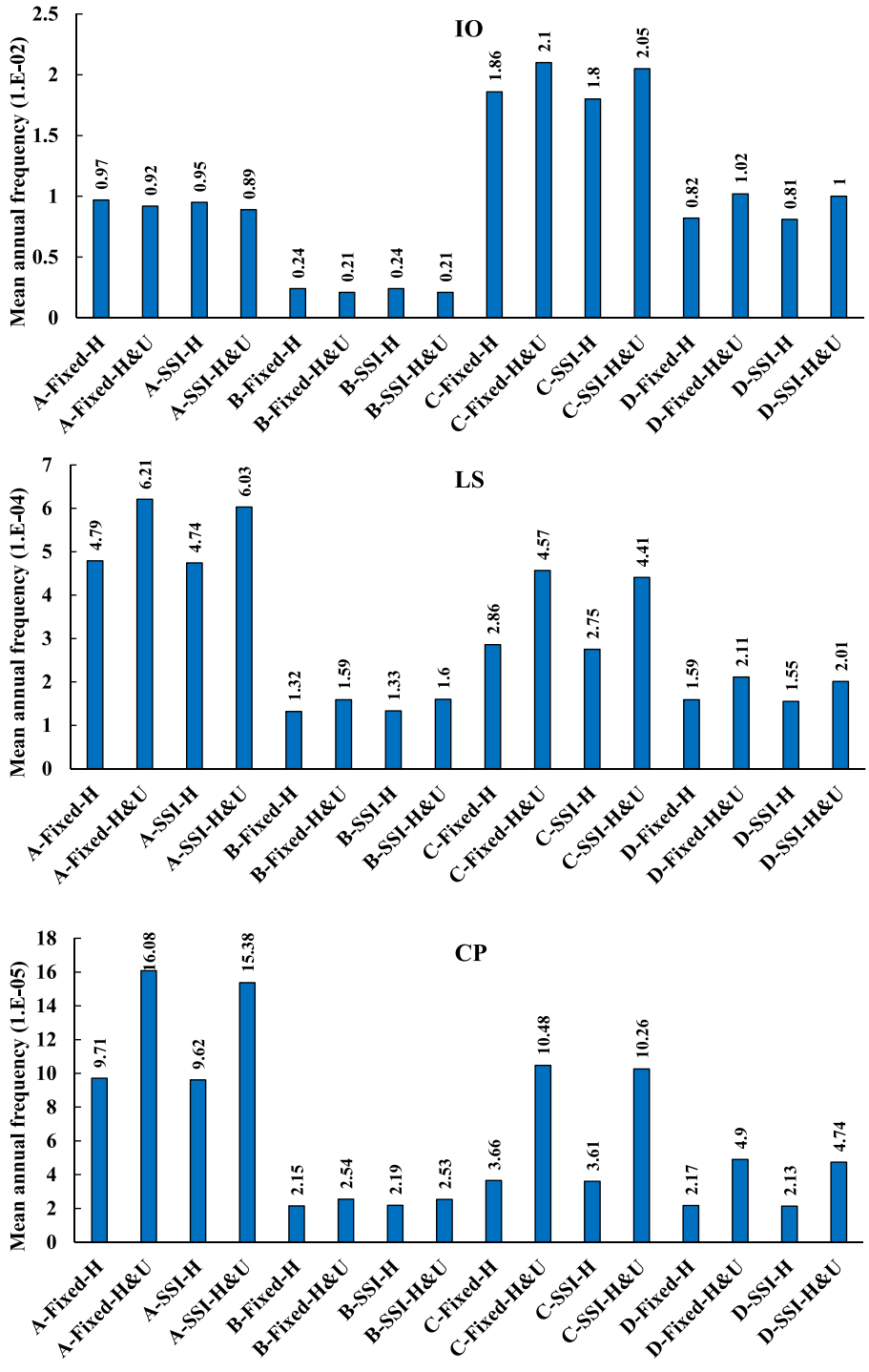

Fig. 11. MAF for the studied SGFs at the IO, LS and CP limit states.

8. Conclusion

In this study, IDA analysis was performed on four SGFs with spans of 20 m and 60 m and heights of 6 m and 12 m with and without considering the effects of the vertical component of earthquake and SSI for the first time. The results were presented in the form of multi-record IDA curves, summarized IDA curves, fragility curves and PSDA curves. Some of the main findings as the contributions of the present research are as follows:

1. According to the fundamental periods in modal analysis, consideration of SSI caused a slight increase in the fundamental period of SGFs. These slight increases in models A, B, C and D were equal to 0.22, 0.13, 0.32 and 0.15%, respectively.
2. According to the multi-record IDA curves, considering the vertical component of earthquake caused the structure to reach the nonlinear region more quickly, enlarged the data dispersion and demand sensitivity, raised the stiffness changes in the nonlinear region and intensified the softening behavior. However, the consideration of SSI did not significantly change the seismic behavior of SGFs.

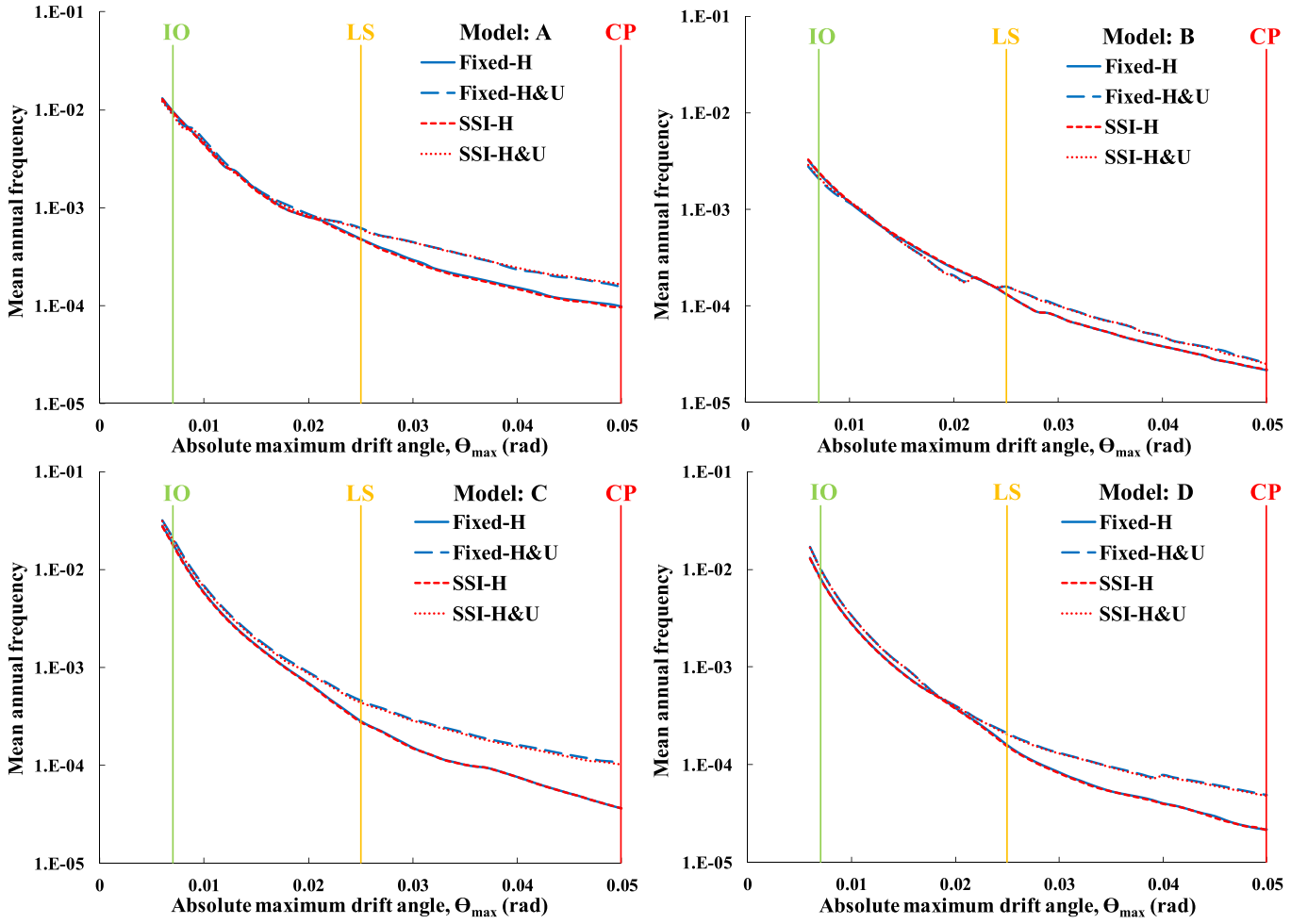

Fig. 12. PSDA curves for the studied SGFs.

3. According to the summarized IDA curves, considering the vertical component of earthquake significantly reduced the dynamic capacity of SGFs, especially when they had wide spans. The largest dynamic capacity reductions in the 50% IDA curves were related to Models D and C with 28 and 22%, respectively. Also, consideration of SSI at all performance levels resulted in a slight increase in the dynamic capacity of SGFs, especially when they had wide spans.
4. According to the fragility curves, considering the vertical component of earthquake increased the failure probability of SGFs and accelerated the damage in them, especially when they had wide spans. Also, considering SSI at all performance levels, on average, slightly reduced the failure probability of SGFs, especially when they had wide spans.
5. According to the MAF of the limit states and PSDA curves, considering the vertical component of earthquake caused a significant increase in the MAF of SGFs, especially when they had wide spans. The highest increases in MAF were related to Models C and D with 186 and 126%, respectively. Also, consideration of SSI at all performance levels led to a slight reduction in the MAF of SGFs, especially when they had wide spans. In addition, under similar conditions, Models A and C had higher MAF than Models B and D.
6. The effect of the vertical component of earthquake in nonlinear regions was much greater than that in the linear regions. So that at the IO performance level, its impact is negligible in short-span SGFs, while it cannot be overlooked with wide-span SGFs. However, the consideration of SSI had almost the same effect on the seismic behavior of SGFs in both the linear and nonlinear regions.
7. Considering the vertical component of earthquake caused a much greater difference in the seismic behavior of SGFs with changing their spans than their heights. This was also the case for the SSI effect on a smaller scale.

In general, the results showed the importance of the vertical component of earthquake on the seismic performance of wide-span SGFs. Disregarding the vertical component of earthquake in the study of wide-span SGFs can lead to a meaningful deviation of the outcomes from the actual results, especially when they are subject to severe earthquakes. Moreover, the results showed that when short-span SGFs are subject to weak earthquakes, the vertical component of earthquake is not much important. Also, SSI does not have any significant role in the seismic performance of SGFs; just partially leading to more conservative results, especially when they have wide spans. In addition, the results of the PSDA analysis showed that under similar conditions, short-period SGFs are more vulnerable than long-period SGFs and should be prioritized for retrofitting.

Declaration of Competing Interest

The authors declare that they have no known competing financial interests or personal relationships that could have appeared to influence the work reported in this paper.

Data availability

Data will be made available on request.

Acknowledgments

This research did not receive any specific grant from funding agencies in the public, commercial, or not-for-profit sectors.

References

[1] F. Jalayer, Direct Probabilistic Seismic Analysis: Implementing Non-linear Dynamic Assessments, Stanford University, California, USA, 2003.
[2] J. Ruiz-Garcia, E. Miranda, Performance-Based Assessment of Existing Structures Accounting for Residual Displacements, Stanford University, California, USA, 2005.
[3] J. Ruiz-Garcia, E. Miranda, Probabilistic estimation of residual drift demands for seismic assessment of multi-story framed buildings, Eng. Struct. 32 (1) (2010) 11–20, https://doi.org/10.1016/j.engstruct.2009.08.010.
[4] Y. Bozorgnia, M. Niazi, K.W. Campbell, Characteristics of free-field vertical ground motion during the Northridge earthquake, Earthquake Spectra 11 (4) (1995) 515–525, https://doi.org/10.1193/1.1585825.
[5] G.Q. Wang, X.Y. Zhou, P.Z. Zhang, et al., Characteristics of amplitude and duration for near fault strong ground motion from the 1999 chi-chi, Taiwan earthquake, Soil Dyn. Earthq. Eng. 22 (1) (2002) 73–96, https://doi.org/10.1016/S0267-7261(01)00047-1.
[6] J. Yang, C.M. Lee, Characteristics of vertical and horizontal ground motions recorded during the Niigata-ken Chuetsu, Japan Earthquake of 23 October 2004, Eng. Geol. 94 (1) (2007) 50–64, https://doi.org/10.1016/j.enggeo.2007.06.003.
[7] J. Xie, X. Li, Z. Wen, et al., Near-source vertical and horizontal strong ground motion from the 20 April 2013 Mw 6.8 Lushan earthquake in China, Seismol. Res. Lett. 85 (1) (2014) 23–33, https://doi.org/10.1785/0220130121.
[8] A.J. Papazoglou, A.S. Elnashai, Analytical and field evidence of the damaging effect of vertical earthquake ground motion, Earthq. Eng. Struct. Dyn. 25 (10) (1996) 1109–1138, https://doi.org/10.1002/(SICI)1096-9845(199610)25:10<1109::AID-EQE604>3.0.CO;2-0.
[9] S. Tanimura, K. Mimura, T. Nonaka, et al., Dynamic failure of structures due to the great Hanshin-Awaji earthquake, International Journal of Impact Engineering 24 (6) (2000) 583–596, https://doi.org/10.1016/S0734-743X(99)00049-4.
[10] S.J. Kim, C.J. Holub, A.S. Elnashai, Experimental investigation of the behavior of RC bridge piers subjected to horizontal and vertical earthquake motion, Eng. Struct. 33 (7) (2011) 2221–2235, https://doi.org/10.1016/j.engstruct.2011.03.013.
[11] G.M. Verderame, D.F. Luca, P. Ricci, et al., Preliminary analysis of a soft-storey mechanism after the 2009 L'Aquila earthquake, Earthq. Eng. Struct. Dyn. 40 (8) (2011) 925–944, https://doi.org/10.1002/eqe.1069.
[12] S.J. Kim, A.S. Elnashai, Characterization of shaking intensity distribution and seismic assessment of RC buildings for the Kashmir (Pakistan) earthquake of October 2005, Eng. Struct. 31 (12) (2009) 2998–3015, https://doi.org/10.1016/j.engstruct.2009.08.001.
[13] H. Lee, K.M. Mosalam, Seismic evaluation of the shear behavior in reinforced concrete bridge columns including effect of vertical accelerations, Earthq. Eng. Struct. Dyn. 43 (3) (2014) 317–337, https://doi.org/10.1002/eqe.2346.
[14] L.D. Sarno, A.S. Elnashai, G. Manfredi, Assessment of RC columns subjected to horizontal and vertical ground motions recorded during the 2009 L'Aquila (Italy) earthquake, Eng. Struct. 33 (5) (2011) 1514–1535, https://doi.org/10.1016/j.engstruct.2011.01.023.
[15] H. Yang, X. Yin, Transient responses of girder bridges with vertical poundings under near-fault vertical earthquake, Earthq. Eng. Struct. Dyn. 44 (15) (2015) 2637–2657, https://doi.org/10.1002/eqe.2601.
[16] Y. Chen, C. Kun, T. Larkin, et al., Impact of vertical ground excitation on a bridge with footing uplift, J. Struct. Eng. 20 (7) (2016) 1035–1053, https://doi.org/10.1080/13632469.2015.1113450.
[17] C.C. Harrington, A.B. Liel, Collapse assessment of moment frame buildings, considering vertical ground shaking, Earthq. Eng. Struct. Dyn. 45 (15) (2016) 2475–2493, https://doi.org/10.1002/eqe.2776.
[18] L. Moschen, R.A. Medina, C. Adam, Vertical acceleration demands on column lines of steel moment-resisting frames, Earthq. Eng. Struct. Dyn. 45 (12) (2016) 2039–2060, https://doi.org/10.1002/eqe.2751.
[19] H. Abdollahiparsa, P. Homami, F. Khoshnoudian, Effect of vertical component of an earthquake on steel frames considering soil-structure interaction, KSCE J. Civ. Eng. 20 (7) (2016) 2790–2801, https://doi.org/10.1007/s12205-016-0687-y.
[20] K. Faramarz, R. Montazar, Seismic response of double concave friction pendulum base-isolated structures considering vertical component of earthquake, Adv. Struct. Eng. 13 (1) (2010) 1–13, https://doi.org/10.1260/1369-4332.13.1.1.
[21] S. Furukawa, E. Sato, Y. Shi, et al., Full-scale shaking table test of a base-isolated medical facility subjected to vertical motions, Earthq. Eng. Struct. Dyn. 42 (13) (2013) 1931–1949, https://doi.org/10.1002/eqe.2305.
[22] A. Bayraktar, E. Hökelekli, F.M. Halifeoğlu, et al., Vertical strong ground motion effects on seismic damage propagations of historical masonry rectangular minarets, Eng. Fail. Anal. 91 (2018) 115–128, https://doi.org/10.1016/j.engfailanal.2018.04.029.
[23] G. Rinaldin, M. Fasan, S. Noé, et al., The influence of earthquake vertical component on the seismic response of masonry structures, Eng. Struct. 185 (2019) 184–193, https://doi.org/10.1016/j.engstruct.2019.01.138.
[24] M.R. Kianoush, J.Z. Chen, Effect of vertical acceleration on response of concrete rectangular liquid storage tanks, Eng. Struct. 28 (5) (2006) 704–715, https://doi.org/10.1016/j.engstruct.2005.09.022.
[25] M.S. Sobhan, F.R. Rofooei, K.A. Attari, Buckling behavior of the anchored steel tanks under horizontal and vertical ground motions using static pushover and incremental dynamic analyses, Thin-Walled Struct. 112 (2017) 173–183, https://doi.org/10.1016/j.tws.2016.12.022.
[26] Z.Y. Chen, W. Chen, W. Zhang, et al., Effects of axial compression ratio of central columns on seismic performance of a multi-story underground structure, Int. J. Comput. Methods 13 (2016) 1641014, https://doi.org/10.1142/S0219876216410140.
[27] W. Li, Q. Chen, Effect of vertical ground motions and overburden depth on the seismic responses of large underground structures, Eng. Struct. 205 (2020) 110073, https://doi.org/10.1016/j.engstruct.2019.110073.
[28] A.S. Veletsos, J.W. Meek, Dynamic behaviour of building-foundation systems, Earthq. Eng. Struct. Dyn. 3 (2) (1974) 121–138, https://doi.org/10.1002/eqe.4290030203.
[29] J.J. Johnson, Soil Structure Interaction: The Status of Current Analysis Methods and Research, Lawrence Livermore National Laboratory, Livermore, California, USA, 1981.
[30] G. Mylonakis, G. Gazetas, Seismic soil-structure interaction: beneficial or detrimental? J. Earthq. Eng. 4 (3) (2000) 277–301, https://doi.org/10.1080/13632460009350372.
[31] M. Lou, H. Wang, X. Chen, Zhai, et al., Structure–soil–structure interaction: literature review, Soil Dyn. Earthq. Eng. 31 (12) (2011) 1724–1731, https://doi.org/10.1016/j.soildyn.2011.07.008.
[32] Y. Xie, R. Desroches, Sensitivity of seismic demands and fragility estimates of a typical California highway bridge to uncertainties in its soil-structure interaction modeling, Eng. Struct. 189 (2019) 605–617, https://doi.org/10.1016/j.engstruct.2019.03.115.
[33] E.N. Tochaei, T. Taylor, F. Ansari, Effects of near-field ground motions and soil-structure interaction on dynamic response of a cable-stayed bridge, Soil Dyn. Earthq. Eng. 133 (2020) 106115, https://doi.org/10.1016/j.soildyn.2020.106115.
[34] O.M. Ramadan, S.S. Mehanny, A.A. Kotb, Assessment of seismic vulnerability of continuous bridges considering soilstructure interaction and wave passage effects, Eng. Struct. 206 (2020) 110161, https://doi.org/10.1016/j.engstruct.2019.110161.
[35] A. Yanik, Seismic control performance indices for magneto-rheological dampers considering simple soil-structure interaction, Soil Dyn. Earthq. Eng. 129 (2020) 105964, https://doi.org/10.1016/j.soildyn.2019.105964.
[36] R. Scarfone, B. Morigi, R. Conti, Assessment of dynamic soil-structure interaction effects for tall buildings: a 3D numerical approach, Soil Dyn. Earthq. Eng. 128 (2020) 105864, https://doi.org/10.1016/j.soildyn.2019.105864.
[37] J. Yang, Z. Lu, P. Li, Large-scale shaking table test on tall buildings with viscous dampers considering pile-soil-structure interaction, Eng. Struct. 220 (2020) 110960, https://doi.org/10.1016/j.engstruct.2020.110960.
[38] F.D. Borbón, M. Domizio, D. Ambrosini, et al., Influence of various parameters in the seismic soil-structure interaction response of a nuclear power plant, Eng. Struct. 217 (2020) 110820, https://doi.org/10.1016/j.engstruct.2020.110820.
[39] S. Kumar, P. Raychowdhury, P. Gundlapalli, Response analysis of a nuclear containment structure with nonlinear soil–structure interaction under bi-directional ground motion, Int. J. Adv. Struct. Eng. 7 (2015) 211–221, https://doi.org/10.1007/s40091-015-0092-7.
[40] L. Bhaumik, P. Raychowdhury, Seismic response analysis of a nuclear reactor structure considering nonlinear soil-structure interaction, Nucl. Eng. Des. 265 (2013) 1078–1090, https://doi.org/10.1016/j.nucengdes.2013.09.037.
[41] A. Banerjee, T. Chakraborty, V. Matsagar, et al., Dynamic analysis of an offshore wind turbine under random wind and wave excitation with soil-structure interaction and blade tower coupling, Soil Dyn. Earthq. Eng. 125 (2019) 105699, https://doi.org/10.1016/j.soildyn.2019.05.038.
[42] S. Austin, S. Jerath, Effect of soil-foundation-structure interaction on the seismic response of wind turbines, Ain Shams Eng. J. 8 (3) (2017) 323–331, https://doi.org/10.1016/j.asej.2017.05.007.
[43] ASCE/SEI 7–10, Minimum Design Loads and Associated Criteria for Buildings and Other Structures, American Society of Civil Engineers in partnership with Structural Engineering Institute, Reston, Virginia, USA, 2010.
[44] AISC 360–10, Specification for Structural Steel Buildings, American Institute of Steel Construction, Chicago, Illinois, USA, 2010.
[45] AISC 341–10, Seismic Provisions for Structural Steel Buildings, American Institute of Steel Construction, Chicago, Illinois, USA, 2010.
[46] M.K. Jafari, Seismic Microzonation of North of Tehran from the Viewpoint of Site Conditions, International Institute of Earthquake Engineering and Seismology, Tehran, Iran, 1999.
[47] M.K. Jafari, Supplementary Studies of Seismic Microzonation of South of Tehran, International Institute of Earthquake Engineering and Seismology, Tehran, Iran, 2002.
[48] P. Raychowdhury, S.R. Chaudhuri, Seismic response of nonstructural components supported by a 4-story SMRF: effect of nonlinear soil–structure interaction, Structures 3 (2015) 200–210, https://doi.org/10.1016/j.istruc.2015.04.006.
[49] ACI 318–-14, Building Code Requirements for Structural Concrete and Commentary, American Concrete Institute, Farmington Hills, Michigan, USA, 2014.
[50] OpenSees, Open System for Earthquake Engineering Simulation, Pacific Earthquake Engineering Research Center. University of California, Berkeley, California, USA, 2018.
[51] A.K. Chopra, Dynamics of Structures: Theory and Applications to Earthquake Engineering, Prentice-Hall, Englewood Cliffs, New Jersey, USA, 2007.
[52] FEMA 356, Prestandard and Commentary for the Seismic Rehabilitation of Buildings, Federal Emergency Management Agency, Washington DC, USA, 2000.

[53] N. Allotey, M.H. Naggar, Analytical moment-rotation curves for rigid foundations based on a Winkler model, Soil Dyn. Earthq. Eng. 23 (5) (2003) 367–381, https://doi.org/10.1016/S0267-7261(03)00034-4.
[54] G. Gazetas, Seismic design of foundations and soil-structure interaction, in: First European Conference on Earthquake Engineering and Seismology. Switzerland, 2006.
[55] C.W. Harden, T. Hutchinson, M. Moore, Investigation into the effects of foundation uplift on simplified seismic design procedures, Earthquake Spectra 22 (3) (2006) 663–692, https://doi.org/10.1193/1.2217757.
[56] J. Thomas, S. Gajan, B. Kutter, Soil-Foundation-Structure Interaction: Shallow Foundations, Center for Geotechnical Modeling, Davis, California, USA, 2005.
[57] J. Zhang, Y. Tang, Radiation damping of shallow foundations on nonlinear soil medium, in: Fourth International Conference on Earthquake Geotechnical Engineering. Greece, 2007.
[58] P. Raychowdhury, Nonlinear Winkler-Based Shallow Foundation Model for Performance Assessment of Seismically Loaded Structures, Ph.D. dissertation, University of California, San Diego, California, USA, 2007.
[59] C.W. Harden, T. Hutchinson, G.R. Martin, et al., Numerical Modeling of the Nonlinear Cyclic Response of Shallow Foundations, Pacific Earthquake Engineering Research Center. University of California, Berkeley, California, USA, 2005.
[60] ATC-40, Seismic Evaluation and Retrofit of Concrete Buildings, Applied Technology Council (ATC), Redwood City, California, USA, 1996.
[61] R.W. Boulanger, The PySimple1, QzSimple1, and TzSimple1 Material Documentation for the OpenSees Platform [<Available at, http://opensees.berkeley.edu, 2000.
[62] K. Terzaghi, Theoretical Soil Mechanics, Wiley, New York, USA, 1943.
[63] G.G. Meyerhof, Some recent research on the bearing capacity of foundations, Can. Geotech. J. 1 (1) (1963) 16–26, https://doi.org/10.1139/t63-003.
[64] H. Reissner, Zum erddruckproblem, in: Proceedings, first international congress of applied mechanics. Delft, Netherlands, 1924, pp. 295–311.
[65] L. Prandtl, Uber die eindringungsfestigkeit harte plastischer baustoffe and die festigkeit von schneiden, Z. Angew. Math. Mech. 1 (1) (1921) 15–20, https://doi.org/10.1002/zamm.19210010102.
[66] G. Gazetas, Foundation Vibrations, Foundation engineering handbook, Van Nostrand Reinhold, New York, USA, 1991.
[67] SAP2000, Version 19.2.2. Analysis Reference Manual, Computers and Structures Inc, Berkeley, California, USA, 2018.
[68] FEMA P695, Quantification of Building Seismic Performance Factors, Federal Emergency Management Agency, Washington DC, USA, 2009.
[69] N. Shome, C.A. Cornell, Probabilistic Seismic Demand Analysis of Nonlinear Structures. Report No. RMS-35, Stanford University, California, USA, 1999.
[70] PEER-NGA Database, Pacific Earthquake Engineering Research Center, University of California, Berkeley, California, USA, 2006 [<Available at, https://peer.berkeley.edu/nga/.
[71] S. Antoniou, R. Pinho, F. Bianchi, SeismoSignal. Version 3.2.0, 2008.
[72] D. Vamvatsikos, C.A. Cornell, Applied incremental dynamic analysis, Earthquake Spectra 20 (2) (2004) 523–553, https://doi.org/10.1193/1.1737737.
[73] N. Luco, Probabilistic Seismic Demand Analysis, SMRF Connection Fractures, and near-Source Effects, Ph.D. dissertation, University of California, Stanford, California, USA, 2002.
[74] D. Vamvatsikos, Derivation of new SAC/FEMA performance evaluation solutions with second-order hazard approximation, Earthq. Eng. Struct. Dyn. 42 (8) (2013) 1171–1188, https://doi.org/10.1002/eqe.2265.
[75] Y. Gholipoor, Y. Bozorgnia, M. Rahnama, et al., Probabilistic Seismic Hazard Analysis Phase I Tehran Regions Final Report, Engineering Optimization Research Group. University of Tehran, Tehran, Iran, 2009 [<Available at, https://iranhazard.mporg.ir/.